

REPORT DOCUMENTATION PAGE			Form Approved OMB NO. 0704-0188		
<p>The public reporting burden for this collection of information is estimated to average 1 hour per response, including the time for reviewing instructions, searching existing data sources, gathering and maintaining the data needed, and completing and reviewing the collection of information. Send comments regarding this burden estimate or any other aspect of this collection of information, including suggestions for reducing this burden, to Washington Headquarters Services, Directorate for Information Operations and Reports, 1215 Jefferson Davis Highway, Suite 1204, Arlington VA, 22202-4302. Respondents should be aware that notwithstanding any other provision of law, no person shall be subject to any penalty for failing to comply with a collection of information if it does not display a currently valid OMB control number.</p> <p>PLEASE DO NOT RETURN YOUR FORM TO THE ABOVE ADDRESS.</p>					
1. REPORT DATE (DD-MM-YYYY) 21-11-2012		2. REPORT TYPE Final Report		3. DATES COVERED (From - To) 15-Jun-2009 - 14-Sep-2012	
4. TITLE AND SUBTITLE Transient High-Pressure Fuel Injection Processes			5a. CONTRACT NUMBER W911NF-09-1-0208		
			5b. GRANT NUMBER		
			5c. PROGRAM ELEMENT NUMBER 611102		
6. AUTHORS William A. Sirignano, Dorrin Jarrahbashi			5d. PROJECT NUMBER		
			5e. TASK NUMBER		
			5f. WORK UNIT NUMBER		
7. PERFORMING ORGANIZATION NAMES AND ADDRESSES University of California - Irvine Office of Research The Regents of the University of California Irvine, CA 92697 -7600			8. PERFORMING ORGANIZATION REPORT NUMBER		
9. SPONSORING/MONITORING AGENCY NAME(S) AND ADDRESS(ES) U.S. Army Research Office P.O. Box 12211 Research Triangle Park, NC 27709-2211			10. SPONSOR/MONITOR'S ACRONYM(S) ARO		
			11. SPONSOR/MONITOR'S REPORT NUMBER(S) 55367-EG.6		
12. DISTRIBUTION AVAILABILITY STATEMENT Approved for Public Release; Distribution Unlimited					
13. SUPPLEMENTARY NOTES The views, opinions and/or findings contained in this report are those of the author(s) and should not be construed as an official Department of the Army position, policy or decision, unless so designated by other documentation.					
14. ABSTRACT The transient behavior of the jet emerging from the orifice during the start-up and shut-down portion of a typical high-pressure diesel-engine fuel injection is addressed in the present work. The liquid jet injected into air at high pressure has been simulated during start-up, steady-state, and shut-down. Use has been made of an unsteady axisymmetric code with a finite-volume solver of the Navier-Stokes equations for liquid streams and adjacent gas, a boundary-fitted-gridding scheme, and a level-set method for liquid/gas interface tracking. Full jet calculations and					
15. SUBJECT TERMS Fuel injection, hydrodynamic instability, liquid jet, atomization					
16. SECURITY CLASSIFICATION OF:		17. LIMITATION OF ABSTRACT		15. NUMBER OF PAGES	
a. REPORT UU	b. ABSTRACT UU	c. THIS PAGE UU	UU	19a. NAME OF RESPONSIBLE PERSON William Sirignano	
				19b. TELEPHONE NUMBER 949-824-3700	

## Report Title

Transient High-Pressure Fuel Injection Processes

### ABSTRACT

The transient behavior of the jet emerging from the orifice during the start-up and shut-down portion of a typical high-pressure diesel-engine fuel injection is addressed in the present work. The liquid jet injected into air at high pressure has been simulated during start-up, steady-state, and shut-down. Use has been made of an unsteady axisymmetric code with a finite-volume solver of the Navier-Stokes equations for liquid streams and adjacent gas, a boundary-fitted-gridding scheme, and a level-set method for liquid/gas interface tracking. Full jet calculations and analysis have been made. In addition, to ease the resolution problem and capture the shortest unstable surface wavelengths, a new model has been developed to examine stream-wise segments of the jet during transients. The frame of reference has been transferred from the laboratory frame to an accelerating frame fixed to the liquid. This transformation generates a new term as a generalized body force analogous to gravity in equations of motion. Periodic conditions before and aft of the segment are used in this liquid-segment model. Consistent results follow from the two approaches.

The acceleration of the liquid during start-up is about  $10^6 \text{ m/s}^2$  at the orifice exit for high Reynolds numbers. When the jet emerges from the orifice, drag forces due to the dense ambient air cause a deceleration. The classical "mushroom" cap for the developing jet is shredded and non-existent at high Reynolds number. Also, the dynamic protrusions from the jet surface created by shear instability are subject to local accelerations that lead to Rayleigh-Taylor (RT) instability. The higher the Weber and the Reynolds numbers, the shorter the unstable surface wavelengths which appear; so, the more challenging is the resolution problem. Effects of the acceleration, surface tension, and liquid viscosity on the interface instability have been investigated.

The initial disturbances at the interface, i.e., 70-120 microns grow and thin ligaments form at the interface as the gas accelerates above the liquid. RT wavelengths about 10-20 microns sit at the back of these protrusions for both the full jet and liquid segment analyses. Increasing the magnitude of the acceleration leads to longer and thinner ligaments or sheets drawn out of the liquid for higher Weber numbers. The KH wavelengths become as long as 200 microns as the boundary layers develop in both phases and the secondary instability waves become longer, i.e., 20-35 microns. Therefore, the RT instability is not independent of the KH instability for the transient liquid jet. The nonlinear synergism between the longer, highly distorted KH surface waves and the shorter RT waves explains the experimental results that droplet sizes are usually smaller than KH wavelengths and very close to the RT wavelengths appear as a secondary instability on top of KH instability. The range of RT wavelengths for both full jet and liquid-segment model shows a good agreement with the classical instability theories.

---

**Enter List of papers submitted or published that acknowledge ARO support from the start of the project to the date of this printing. List the papers, including journal references, in the following categories:**

**(a) Papers published in peer-reviewed journals (N/A for none)**

<u>Received</u>	<u>Paper</u>
-----------------	--------------

**TOTAL:**

**Number of Papers published in peer-reviewed journals:**

---

**(b) Papers published in non-peer-reviewed journals (N/A for none)**

Received          Paper

**TOTAL:**

**Number of Papers published in non peer-reviewed journals:**

---

**(c) Presentations**

**Number of Presentations:**      0.00

---

**Non Peer-Reviewed Conference Proceeding publications (other than abstracts):**

Received          Paper

08/28/2011    4.00    Dorrin Jarrahbashi, William A. Sirignano, Sadegh Dabiri. Transient High-Pressure Fuel Injection Processes, ILASS Americas Meeting, May, 2011. 2011/05/15 03:00:00, . . . ,

**TOTAL:**                    **1**

**Number of Non Peer-Reviewed Conference Proceeding publications (other than abstracts):**

---

**Peer-Reviewed Conference Proceeding publications (other than abstracts):**

Received          Paper

**TOTAL:**

**Number of Peer-Reviewed Conference Proceeding publications (other than abstracts):**

---

**(d) Manuscripts**

Received      Paper

**TOTAL:**

**Number of Manuscripts:**

---

**Books**

Received      Paper

**TOTAL:**

**Patents Submitted**

---

**Patents Awarded**

---

**Awards**

William A. Sirignano, Wyld Propulsion Award, 2009, American Institute of Aeronautics and Astronautics. Citation "For extensive and fundamental contributions to the advancement of chemical rocket propulsion through theories of nonsteady combustion and fluid dynamics."

---

William A. Sirignano, Society for Industrial and Applied Mathematics Fellow, 2009. Citation; For contributions to fluid dynamics, combustion theory, and their applications to propulsion.

---

**Graduate Students**

<u>NAME</u>	<u>PERCENT SUPPORTED</u>	Discipline
Dorin Jarrahbashi	0.49	
<b>FTE Equivalent:</b>	<b>0.49</b>	
<b>Total Number:</b>	<b>1</b>	

---

**Names of Post Doctorates**

<u>NAME</u>	<u>PERCENT SUPPORTED</u>
<b>FTE Equivalent:</b>	
<b>Total Number:</b>	

---

**Names of Faculty Supported**

<u>NAME</u>	<u>PERCENT SUPPORTED</u>	National Academy Member
William A. Sirignano	0.10	Yes
<b>FTE Equivalent:</b>	<b>0.10</b>	
<b>Total Number:</b>	<b>1</b>	

**Names of Under Graduate students supported**

<u>NAME</u>	<u>PERCENT SUPPORTED</u>
<b>FTE Equivalent:</b>	
<b>Total Number:</b>	

**Student Metrics**

This section only applies to graduating undergraduates supported by this agreement in this reporting period

- The number of undergraduates funded by this agreement who graduated during this period: ..... 0.00
- The number of undergraduates funded by this agreement who graduated during this period with a degree in science, mathematics, engineering, or technology fields:..... 0.00
- The number of undergraduates funded by your agreement who graduated during this period and will continue to pursue a graduate or Ph.D. degree in science, mathematics, engineering, or technology fields:..... 0.00
- Number of graduating undergraduates who achieved a 3.5 GPA to 4.0 (4.0 max scale):..... 0.00
- Number of graduating undergraduates funded by a DoD funded Center of Excellence grant for Education, Research and Engineering:..... 0.00
- The number of undergraduates funded by your agreement who graduated during this period and intend to work for the Department of Defense ..... 0.00
- The number of undergraduates funded by your agreement who graduated during this period and will receive scholarships or fellowships for further studies in science, mathematics, engineering or technology fields: ..... 0.00

**Names of Personnel receiving masters degrees**

<u>NAME</u>
<b>Total Number:</b>

**Names of personnel receiving PHDs**

<u>NAME</u>
<b>Total Number:</b>

**Names of other research staff**

<u>NAME</u>	<u>PERCENT SUPPORTED</u>
<b>FTE Equivalent:</b>	
<b>Total Number:</b>	

**Sub Contractors (DD882)**

**Inventions (DD882)**

**Scientific Progress**

The behavior of the liquid jet injected into air at 30 atm has been simulated during start-up, steady-state, and shut-down. Use has been made of an unsteady axisymmetric code with a finite-volume solver of the Navier-Stokes equations for liquid streams and adjacent gas, a boundary-fitted-gridding scheme, and a level-set method for liquid/gas interface tracking.

The development of the transient jet into the gas involves strong instabilities along the edges and moving front of the transient jet. The simulation of the full jet depicts that, for lower Reynolds numbers, the starting liquid jet forms a cap which grows in volume as it moves downstream and decelerates along the gas chamber. However, for higher Reynolds numbers the mushroom-shaped cap deforms drastically within a few microseconds after the start of injection and KH and RT instabilities develop on the liquid/gas interface. The simulations show that the primary KH wavelengths are on the order of 100-300 microns. As the waves convected downstream, their amplitude increases and long ligaments are drawn out of the liquid. These ligaments further roll back and entrain air during the process, forming significant vortex structures. This behavior of the jet during transients is in good agreement with experimental observations of the transient liquid jet.

At high Reynolds and Weber numbers, small-scale wavelengths and protrusions become even smaller due to exposure to high accelerations normal to their interface. This leads to small-scale RT waves at the edge of the ligaments. The normal acceleration on the fingers is of the order of  $10^6$  m/s<sup>2</sup> and the RT wavelengths are between 10 to 50 microns and increase as the primary KH wavelength become longer. During the start-up, the liquid jet is accelerated into the gas; RT instabilities appear at the rear side of the jet front. However, during shut-down the jet front decelerates. So, the lighter fluid is accelerating into the heavier fluid which is stabilizing on the rear side of the emerging jet and destabilizing on the jet front. A comparison between the computed RT wavelengths with classical linear instability theory shows a reasonable agreement. However, the measured wavelengths are longer compared to the theory due to the fact that the damping effects of viscosity on the smallest wavelengths have not been considered in the theory. The range of unstable wavelengths is consistent with VPF instability analysis that predicts stability for sub-micron and super millimeter wavelengths for the same fluid properties. Unstable wavelength increase up to 1200 microns during the steady-state portion of injection that is larger compared to start-up. At higher Weber and Reynolds numbers, smaller waves and thinner ligaments appear at the liquid/gas interface.

To tackle the resolution problem and capture the shortest unstable surface wavelengths, a new model has been developed to examine stream-wise segments of the jet during transients. The frame of reference has been transferred from the laboratory frame to an accelerating frame fixed to the liquid. This transformation generates a new term as a generalized body force analogous to gravity in equations of motion. The magnitude of the acceleration is derived from full transient jet computations. Periodic conditions fore and aft of the segment are used in this liquid-segment model.

The initial disturbances at the interface, i.e., 70-120 microns grow and thin ligaments form at the interface as the gas accelerates above the liquid. RT wavelengths about 10-20 microns sit at the back of these fingers similar to the scenario described for the full jet. Increasing the magnitude of the acceleration leads to longer and thinner ligaments drawn out of the liquid for higher Weber numbers. The KH wavelengths become as long as 200 microns as the boundary layers develop in both phases and the secondary instability waves become longer, i.e., 20-35 microns. Therefore, the RT instability is not independent of the KH instability for the transient liquid jet. The nonlinear synergism between the longer, highly distorted KH surface waves and the shorter RT waves explains the experimental results that droplet sizes are usually smaller than KH wavelengths and very close to the RT wavelengths appear as a secondary instability on top of KH instability. The range of unstable wavelengths and the unstable structures appearing at the liquid/gas interface repeat the scenario described for full transient jet.

### **Technology Transfer**

ARO Grant W911NF-09-1-0208  
TRANSIENT HIGH-PRESSURE FUEL  
INJECTION PROCESSES

William A. Sirignano, Principal Investigator  
Final Report November 21, 2012  
Submitted to Dr. Ralph A. Anthenien, Jr.,  
Program Manager

Prepared by William A. Sirignano and Dorrin Jarrahbashi  
Department of Mechanical and Aerospace Engineering  
University of California, Irvine 92697-3975

## **Summary**

The transient behavior of the jet emerging from the orifice during the start-up and shut-down portion of a typical high-pressure diesel-engine fuel injection is addressed in the present work. The liquid jet injected into air at high pressure has been simulated during start-up, steady-state, and shut-down. Use has been made of an unsteady axisymmetric code with a finite-volume solver of the Navier-Stokes equations for liquid streams and adjacent gas, a boundary-fitted-gridding scheme, and a level-set method for liquid/gas interface tracking. Full jet calculations and analysis have been made. In addition, to ease the resolution problem and capture the shortest unstable surface wavelengths, a new model has been developed to examine stream-wise segments of the jet during transients. The frame of reference has been

transferred from the laboratory frame to an accelerating frame fixed to the liquid. This transformation generates a new term as a generalized body force analogous to gravity in equations of motion. Periodic conditions before and aft of the segment are used in this liquid-segment model. Consistent results follow from the two approaches.

The acceleration of the liquid during start-up is about  $10^6$  m/s<sup>2</sup> at the orifice exit for high Reynolds numbers. When the jet emerges from the orifice, drag forces due to the dense ambient air cause a deceleration. The classical "mushroom" cap for the developing jet is shredded and non-existent at high Reynolds number. Also, the dynamic protrusions from the jet surface created by shear instability are subject to local accelerations that lead to Rayleigh-Taylor (RT) instability. The higher the Weber and the Reynolds numbers, the shorter the unstable surface wavelengths which appear; so, the more challenging is the resolution problem. Effects of the acceleration, surface tension, and liquid viscosity on the interface instability have been investigated.

The initial disturbances at the interface, i.e., 70-120  $\mu\text{m}$  grow and thin ligaments form at the interface as the gas accelerates above the liquid. RT wavelengths about 10-20  $\mu\text{m}$  sit at the back of these protrusions for both the full jet and liquid segment analyses. Increasing the magnitude of the acceleration leads to longer and thinner ligaments or sheets drawn out of the liquid for higher Weber numbers. The KH wavelengths become as long as 200  $\mu\text{m}$  as the boundary layers develop in both phases and the secondary instability waves become longer, i.e., 20-35  $\mu\text{m}$ . Therefore, the RT instability is not independent of the KH instability for the transient liquid jet. The nonlinear synergism between the longer, highly distorted KH surface waves and the shorter RT waves explains the experimental results that droplet sizes are usually smaller than KH wavelengths and very close to the RT wavelengths appear as a secondary instability on top of KH instability. The range of RT wavelengths for both full jet and liquid-segment model shows a good agreement with the classical instability theories.

# Contents

Title	1
Summary	2
Contents	3
1. Introduction and Literature Review	4
2. Computational Method	9
3. Full Transient Jet	13
<i>3.1 Navier-Stokes and Level-Set Analysis</i>	13
<i>3.2 Instability Analysis</i>	27
4. Liquid-Segment Model	31
5. Conclusions	40
References	42

# 1 Introduction and Literature Review

Understanding, insights, and quantitative descriptions are needed to explain the factors that relate to the mechanisms for the break-up of injected liquid streams at high pressure during transients (e.g., start-up and shut-down). The duration of the start-up and shut-down periods of jet injection will vary from ten to fifty percent of the injection duration, being higher at lighter loads. Consider for example the injection system of a typical heavy-duty Class 8 engine with power in the 150-800 HP range. At heavy load (i.e., high power) and about 2000 rpm, with jet velocity about 300-400 m/s, the valve opens over 40 crank-angle degrees. This converts to about 3.3 milliseconds. The start-up transient covers about 2-4 crank-angle degrees or 0.16 to 0.33 milliseconds. The shut-down transient covers 1-3 crank-angle degrees or 0.08 to 0.25 milliseconds. Fluid in the jet travels the order of several centimeters in a time of order 0.25-0.33 milliseconds. At light load (e.g., 20-25 max power) and about 800 rpm, with jet velocity about 200 m/s the valve opens over 10 crank-angle degrees or 2.1 milliseconds. The start-up transient is 2-3 crank-angle degrees or 0.42 to 0.63 milliseconds. The shut-down transient is 1-2 crank-angle degrees or 0.21 to 0.42 milliseconds and fluid in the jet can travel about 5 cm in time or about 0.25 milliseconds. Therefore, transient behavior becomes more significant as the load decreases (private communication with Dr. Peter Schihl of the U.S. Army Tank and Automotive Command.)

From what is stated above, we see that a better understanding of the transient behavior of a diesel engine is essential to control the temporal variations in the fuel/air mixing process and eventually enhancing the combustion process in an engine. Investigating the liquid/gas interface dynamics of the fuel/air mixture in the early stages of the start of injection and shortly before the end of injection is very challenging. From the experimental scope the dense cloud of droplets and vapor surrounding the fuel jet and very small length and time scales of atomization process makes the optical access to the jet very difficult. Therefore, there is a lack of knowledge regarding the transient behavior of the fuel/air mixture, especially, very close to the nozzle exit. On the other hand, theoretical/computational investigations may lack sufficient resolution for high Reynolds and Weber number ranges that must be treated. For example, the Weber number range can be estimated to be  $10^4$  or higher based on the values for the engine application: (jet velocity= 200-300 m/s; gas density=  $O(100 \text{ kg/m}^3)$ ; jet diameter=  $O(10^{-4} \text{ m})$ ; surface tension coefficient  $O(10^{-2} \text{ N/m})$ ) This will create some challenge in obtain-

ing the needed resolution. However, although Re number is of  $O(10^4)$ , the flow is transitional and not fully established turbulent flow. Thin boundary layers are formed in the orifice at these Re values and the liquid jet begins with thin shear layers.

The transient behavior of liquid injection has been the subject of numerous experimental and numerical studies. Different experimental techniques have been used in the literature to detect the differences between the jet structures during the transient period of injection compared to the steady state period (1; 2; 3; 4; 5; 6). The optical measurement techniques such as shadowgraph and Schlieren imaging and laser-based techniques, e.g., Mie scattering imaging and laser-induced fluorescence produce obscure images from the regions of high droplet density near the nozzle since the light scatters from the surface of the droplets. Therefore, these methods lack the sufficient detailed information about the spray structures near the nozzle; so, further investigations in this field seems necessary.

Smallwood *et al.* (7) and Gulder (8) studied the internal structure of intermittent and highly transient dense diesel sprays using two-dimensional laser light scattering and transmission techniques. They reported noticeable and different near-field structures of the transient jet compared with its steady counterpart. However, the transient jet nearly resembles the steady jet development at further positions downstream of the nozzle. At about 25-30 nozzle diameters, the transient jet has an intermittent structure of dense fluid particles.

Analysis of the transient diesel spray based on the Phase Doppler Particle Analyzer (PDPA) technique by Kim and Lee (9) depicted that, unlike the continuous sprays, the development of spray structure was a time-dependent process for the transient jet. They measured the Sauter Mean Diameter (SMD) for the whole flow field for the time-dependent jet. The SMD gradually increased with time after injection and decreased after reaching a maximum value. They also reported that the need for a broader study to capture the detailed information on the droplet formation process for transient diesel sprays is required for high pressure combustion chambers at very high Re and We numbers.

The ballistic imaging technique provides better images from the near nozzle structures compared to other optical techniques. The behavior of a single diesel spray during the injection process was observed by Linne *et al.* (10) via ballistic imaging techniques. Their results confirmed the appearance of periodic structures and distinct and intermittent voids at the interface very

close to the nozzle exit after about  $10 \mu\text{s}$  of the start of injection. More regular periodic structures at the interface and uniformly-sized voids together with a constant width core revealed the characteristics of steady sprays after about  $100 \mu\text{s}$ . The periodic lengths were slightly greater than the orifice diameter shortly after the injection and increased up to twice the diameter later in time. X-ray radiography techniques have been successfully applied to find the internal mass distribution of a diesel spray. However, the two-dimensional images of high-pressure fuel spray published so far does not reveal the small-scale structures of the near nozzle and high droplet density regions of the spray (2; 11; 4; 5).

Most of the numerical studies on transient jet behavior are based on the extension of the steady-state jet simulations that in turn is dependent on empirical constants obtained from the experiments, e.g., Abania and Reitz (12) formulated a new model for unsteady axisymmetric turbulent jets based on an extension of steady-state gas-jet theory that is shown to be consistent with Helmholtz's vortex-model. Turner *et al.* (13; 14) predicted the transient jet break-up length and its penetration into the gas by modifying the break-up model previously used for axisymmetric steady jets. Their results showed better agreement with the experimental data compared with the other break-up models. From their investigations, the value of acceleration indicates the time required for the amplitudes and wavelengths of the unstable waves to reach the critical criterion for break-up. They also showed that the transient behavior of the jet plays an insignificant role in the overall break-up length of the jet. However, the transient phase of the jet is crucial in the initial stripping of the droplets from the coherent jet. Aneja and Abraham (15) used an axisymmetric model to study the penetration of the liquid fuel in a constant volume chamber under normal diesel engine conditions. Their analysis showed sensitivity to the numerical resolution which had been related to a dependence of the computed Sauter Mean Radius (SMR) of the drops on the grid resolution.

The three-dimensional simulation of primary atomization of turbulent liquid jets using the Refined Level Set Grid (RLSG) method by Herrmann (16) showed that turbulence appears to be the driving mechanism or at least initiator of atomization within the first 20 diameters downstream of the injector. During atomization, the phase interface exhibits a highly complex, three-dimensional surface with a large range of different scales. They admitted that prediction of very small-scale wavelengths during start-up and shut-down is mesh-size dependent even by using RLSG method. This short-

coming has also been indicated by Goroshovski and Herrmann (17).

Liquid-fuel injection systems operate under conditions of high Weber numbers induced by the huge velocity of the jet and high Reynolds numbers. Our challenge is to understand the mechanisms of jet flow under these extreme conditions which lead to the formation of small drops and mist. The disintegration of liquid jets can be framed in terms of instabilities. The instabilities are well known to be critical in the distortion of the liquid/gas interface and in the process by which ligaments of liquid are torn from the jet core. Three kinds of instabilities that can lead to break-up are capillary instability, Kelvin-Helmholtz (KH) instability (an approximation to shear instability) , and Rayleigh-Taylor (RT) instability. The effects of large accelerations superimposed on large velocity differences are possibly an essential feature in liquid fuel injection systems and a major cause of RT instability. As the jet emerges from the orifice, drag forces due to entry into the dense air cause a deceleration. Also, the dynamic protrusions from the jet surface are subject to accelerations. The signature of this instability is the waves that corrugate at the free surface at the instant of acceleration. Ultimately, these waves will finger into the liquid causing it to break-up. There has been a lack of knowledge in the literature regarding the effects of RT instabilities on jet break-up during start-up and shut-down transients.

Studying the mechanisms involved in secondary instability and break-up of droplets due to acceleration could be very promising to predict the effects of acceleration on liquid streams. Varga *et al.* (18) described the break-up of a small diameter liquid jet exposed to high-speed gas jet as secondary RT instability of the primary KH instability. They proposed a phenomenological break-up model for the initial droplet size based on the same acceleration mechanism that breaks up liquid drops in high speed airstream investigated by Joseph and co-workers (19; 20). Varga *et al.* (18) observed that RT instability was generated on the wave crests resulted from the primary KH instability. Their model assumes that liquid is inviscid. In fact, the RT instability depends strongly on viscosity and the effects of viscosity are remarkably well represented by Viscous Potential Flow (VPF) instability analysis (21; 22).

Joseph *et al.* (20) investigated the secondary break-up of both Newtonian and non-Newtonian droplets in a shock tube exposed to very high accelerations of orders  $10^4$  to  $10^5$  times the gravity. They claimed that the Rayleigh-Taylor (RT) instability is the main cause of the break-up. Han and Tryggvason (23) performed a numerical simulation of the secondary break-up of droplets exposed to both impulsive and constant body force acceleration

for low-density ratios. They added a body force to the axisymmetric Navier-Stokes equations to simulate the effects of constant acceleration on droplet surface. They claimed that acceleration controls the break-up mechanism when the viscous effects are negligible and surface tension is constant. The study of the break-up mode revealed that for higher accelerations the drop is deformed into a very thin film pulled in the downstream direction; that is an indication of the shear break-up mode. Therefore, the secondary instability (RT) due to very high accelerations in transient jet indicates the size of the smallest liquid ligaments that finally will break-up from the liquid core and form the droplets. Thus, the estimations of the smallest wavelengths at the liquid/gas interface can be promising in predicting the droplet size distribution for jet atomization under very severe conditions.

The first part of this work concentrates on the numerical simulation of a single transient axisymmetric jet injected into high pressure quiescent air at very high We and Re numbers during start-up, steady-state, and shut-down portions of the injection. The jet instabilities during the start-up period in the near nozzle region, where the length of the jet is less than 5 orifice diameters, are of great importance. This region is of interest due to very high accelerations that the liquid jet experiences as the pressure is increasing in the orifice. Simultaneously, the mushroom-shaped cap forms and develops due to the effects of drag forces acting on the liquid. Finally, the amalgamation of various physical mechanisms leads to highly complicated instability structures on the jet interface and the cap. Therefore, the near nozzle region during start-up will be treated carefully in this paper.

The valuable information obtained from the full transient jet simulations will be used to develop a new model to capture the instabilities at the liquid/air interface with better resolution. These simulations can be extremely costly if the full jet is being considered numerically. In this new model, a segment of the jet whose fixed length is longer than the interesting wavelengths but still computationally manageable will be considered during the start-up period of injection. Some comparisons with the classical instability theories and full jet simulations will be made to verify the usefulness of the Liquid-Segment model for the various configurations and conditions under study.

Although a three-dimensional simulation of a liquid jet injected into high pressure environment provides more detailed information on jet break-up (16), the axisymmetric liquid-segment model presented in this paper opens a new gateway for reducing the simulation costs for severe flow conditions, e.g.,

high  $Re$  and high  $We$  numbers. Once this axisymmetric model is established and proved to be helpful in predicting the transient liquid jet instability, developing a three-dimensional model will be the very next goal to follow in future.

This paper’s approach will center on the development and use of theoretical and computational models to solve the unsteady, multi-dimensional Navier-Stokes equations for flow through injection and the exiting transient jet through orifice. Use will be made of the previously developed unsteady multidimensional code with the finite-volume solver of the Navier-Stokes equations for liquid streams and adjacent gas, boundary-fitted-gridding scheme, and level-set method for liquid/gas interface tracking applied by (24; 25; 26). We will use the model capability to examine the orifice and jet flows during start-up and shut-down transition, typical of intermittent combustors, predicting jet formation and resulting axisymmetric instabilities that can lead to stream break-up. In the proposed model, the observations from the experiments of (10) based on near field ballistic images of a diesel spray during the start-up, steady-state, and shut-down will provide some guidance to describe the phenomena observed in our numerical simulation. The Viscous Potential Flow (VPF) instability theories will also be applied as a mean to validate the range of unstable wavelengths observed in our simulations.

## 2 Computational Method

The Navier-Stokes and continuity equations for an incompressible flow follows:

$$\rho \frac{\partial \mathbf{u}}{\partial t} + \rho(\mathbf{u} \cdot \nabla)\mathbf{u} = -\nabla p + \mu \nabla^2 \mathbf{u} + \mathbf{F}; \quad \nabla \cdot \mathbf{u} = 0 \quad (1)$$

where  $\mathbf{u}$  is the velocity field;  $\rho$  and  $\mu$  are the density and dynamic viscosity of the fluid, respectively.  $p$  is the pressure and  $\mathbf{F}$  is the body force applied to the fluid. We consider a finite volume discretization on a staggered grid. The convection-diffusion problem has been discretized based on the finite volume method using the QUICK algorithm (27) and the Crank-Nicolson scheme for discretizing the unsteady term. The coupling of the continuity and momentum equations is done through the SIMPLE algorithm (28). The level-set method developed by Osher and co-workers (29; 30) is used for tracking the liquid/gas interface. The level-set is defined as a distance function with

zero value at the liquid/gas interface; positive values in the gas phase and negative values in the liquid phase. It is denoted by  $\theta$  and all the fluid properties for both phases in the Navier-Stokes equations can be defined based on their values and the equations could be solved for both phases simultaneously. The level-set function is also convected by the unknown velocity field based on the following equation:

$$\frac{\partial \theta}{\partial t} + \mathbf{u} \cdot \nabla \theta = 0 \quad (2)$$

In addition, the surface tension force applied on the interface is defined based on the level-set function and curvature of the interface as is shown in the third term on the right-hand side of the Navier-Stokes equation as follows:

$$\rho \frac{D\mathbf{u}}{Dt} = -\nabla p + \mu \nabla^2 \mathbf{u} - \sigma \kappa \delta(d) \mathbf{n} \quad (3)$$

where  $\sigma$  is the surface tension coefficient,  $\delta$  is the delta function,  $d$  represents the distance from the interface,  $\mathbf{n}$  and  $\kappa$  are the normal vector directing toward the gas phase and the curvature of the interface, respectively. For detailed descriptions on interface tracking (26).

The computational domain and gridding system that consists of an orifice initially full of liquid and a gas chamber initially filled with quiescent gas is demonstrated in figure 1(a). The plenum pressure upstream in the orifice is set to increase exponentially over a period of 0.3 ms until a prescribed maximum pressure is reached after which the plenum pressure is held constant at that cap value for another 0.1 ms. The plenum pressure drives the flow and the mass flux; the exit velocity of the jet increases with the plenum pressure. At the end of the start-up process, the maximum jet velocity reaches 200 m/s. The no-slip boundary condition on the orifice channel wall and slip condition on the top wall of the gas chamber have been applied. The velocity and viscous stress are continuous at the liquid/gas interface. The computational grid consists of an orthogonal coordinate system based on potential flow solutions in the orifice and a Cartesian coordinate system in the external flow. There are 4000 and 600 mesh points in the x and r-direction, with 9600 mesh points lying in the orifice and orifice channel and 2,390,400 in the external flow. The flow properties are summarized in table 1.

$Re$ ,  $We$ , and  $Fr$  numbers have been defined as follows:  $Re = \frac{\rho_l \bar{u} D}{\mu_l}$ ,  $We = \frac{\rho_l \bar{u}^2 D}{\sigma}$ ,  $Fr = \sqrt{\frac{\bar{u} \tau}{D}} = \frac{\bar{u}}{\sqrt{aD}}$ , where  $\bar{u}$ ,  $\rho_l$ ,  $\mu_l$ ,  $\sigma$ ,  $D$ ,  $a$ , and  $\tau$  are the mean

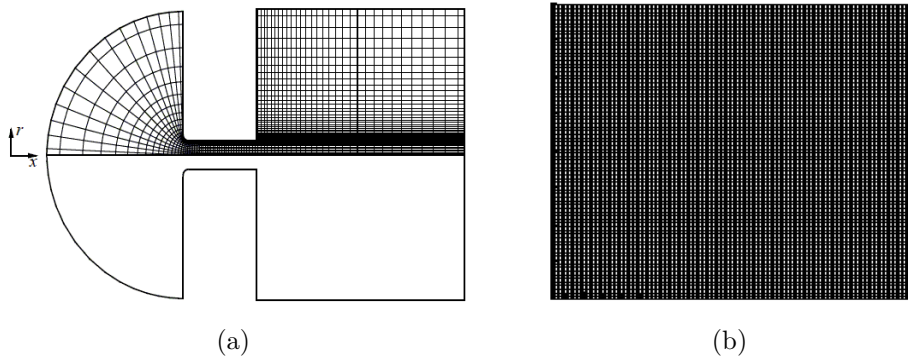


Figure 1: Physical domain and orthogonal grid (a) Orifice and gas chamber for full jet (flow from left to right) (b) liquid-segment model.

<i>FluidProperties</i>	Liquid (Kerosene)	Gas (air)
Viscosity (kg/m.s)	2.7e-3	1.8e-5
Density (kg/m <sup>3</sup> )	804	38.4 at 30 atm
Surface Tension Coefficient (N/m)	0.028	-
Maximum Jet Velocity (m/s)	200	-

Table 1: Fluid properties

exit plane velocity corresponding to the maximum mass flow rate, the liquid density, liquid viscosity, surface tension coefficient, orifice diameter, mean local exit fluid acceleration, and time required for the liquid jet velocity transition from zero to  $\bar{u}$  at the orifice exit, respectively.

Predicting the jet instability during steady-state followed by the shut-down process requires the length of the gas chamber to be more than 200 times the orifice diameter which would increase the cost of the simulations significantly. Therefore, the valuable information obtained from the full transient jet simulations described above has been used to develop a new model to capture the instabilities at the liquid/gas interface with better resolution and lower cost than for the full jet computations. In this new model, a segment of the jet whose fixed length is longer than the interesting wavelengths but still computationally manageable, e.g., 1-mm length for a 200-micron initial diameter will be considered during the start-up period of jet injection. The gridding system and computational domain has been shown in figure 1(b).

To consider the effects of acceleration on the fluid motion of this segment, we transfer the frame of reference from the laboratory frame identified with  $(\mathbf{x}, t)$  and the fluid velocity  $\mathbf{U}(\mathbf{x}, t)$  to an accelerating frame in which the mass center of the segment is stationary, identified with  $(\mathbf{X}, t)$  and  $\mathbf{v}(\mathbf{X}, t)$  where  $\mathbf{v}(\mathbf{X}, t) = \mathbf{U}(\mathbf{x}, t) + \mathbf{V}(t)$  and  $d\mathbf{X} = d\mathbf{x} + \mathbf{V}(t)dt$ .  $\mathbf{V}(t)$  is the liquid injection velocity at the orifice that varies with time only. In other words, we assume that all the liquid particles travel with the same velocity as the liquid jet exit. Substituting  $\mathbf{v}(\mathbf{X}, t) = \mathbf{U}(\mathbf{x}, t) + \mathbf{V}(t)$  in 1 and considering the fact that the spatial derivative of  $\mathbf{V}(t)$  is zero, the resultant modified Navier-Stokes equation is obtained as in Equation (4). This transformation generates a new term  $\rho\dot{\mathbf{V}}$  as a generalized body force analogous to gravity in the equations of motion 4.  $\dot{\mathbf{V}}$  is the acceleration of the frame of reference equivalent to the acceleration of the liquid jet emerging from the orifice.

$$\rho \frac{D\mathbf{U}}{Dt} = -\nabla p + \mu \nabla^2 \mathbf{U} - \sigma \kappa \delta(d) \mathbf{n} - \rho \dot{\mathbf{V}}; \quad \nabla \cdot \mathbf{U} = 0 \quad (4)$$

The fluid segment consists initially of two concentric cylinders; liquid is in the inner cylinder and the gas fills the surrounding outer cylinder. In our first calculations, the diameters of the inner and outer cylinders are 200 and 800  $\mu\text{m}$ , respectively, and the length of the liquid segment is 1 mm. So, the outer gas domain has one order of magnitude of volume more than the liquid domain. The liquid segment diameter is consistent with the jet-orifice diameter used in full jet simulation. The total number of mesh points is 400,000 (1000 in x-direction and 400 in r-direction); the computational grid consists of a uniform mesh ( $\Delta x = \Delta r = 1 \mu\text{m}$ .)

Use will be made of the same scheme used for full jet simulations considering the effects of constant body force given in Equation (4). The liquid is initially stationary and the gas flows over the interface from right to left with a starting value associated with the velocity of the liquid jet on the axis of symmetry and acceleration of the liquid jet obtained from the full jet analysis when the jet has penetrated about 1 mm into the gas. The periodic conditions for pressure and velocity at the right and left boundaries and symmetry boundary condition at the bottom boundary of the computational domain have been applied. In addition, the normal gradient of velocity is zero on the top boundary. The flow conditions are the same as the full transient jet as shown by Jarrahbashi *et al.* (31).

## 3 Full Transient Jet

### 3.1 Navier-Stokes and Level-Set Analysis

The axisymmetric CFD code mentioned in the previous section has been developed to simulate the flow of a liquid through an orifice and the gas chamber during start-up, steady-state, and shut-down period of injection. The fluid properties and the computational domain are shown in table 1 and figure 1(a), respectively. Mesh sizes vary from 1 to 10 microns; finer next to the orifice in the major flow direction and 1 to 2 microns in the radial transverse direction and time step is  $10^{-8}$  s. During start-up, the plenum pressure drives the flow and the mass flux and the exit velocity of the jet increase with the plenum pressure. The maximum mass flux and pressure remain constant for about  $100 \mu\text{s}$  during the steady-state period. During the first  $300 \mu\text{s}$  after the start of injection, jet velocity and orifice pressure difference increase from initial zero values to  $200 \text{ m/s}$  and  $1.6 \text{ MPa}$ , respectively. The air pressure in the gas chamber is  $30 \text{ atm}$  and the orifice diameter is  $200 \mu\text{m}$ . The variation of centerline axial-velocity with time along the jet axis is shown in figure 2. This figure shows that there is a time period between the jet start-up at time equal to zero and the arrival of the jet front at a given downstream position. Obviously, the period becomes longer as downstream distance from the exit increases. After the jet front arrives, there begins a period with increasing jet velocity and orifice pressure drop. This period ends at about  $300 \mu\text{s}$  after start-up. Then, a period of near-steady jet velocity begins. Once the jet has reached a downstream position, the instantaneous velocity there is roughly the same value as the jet exit. During the shut-down period, the centerline velocity decreases from maximum velocity but does not reach zero in this flow configuration.

Figure 3 shows the radial variation of velocity with time at one orifice diameter downstream of the orifice exit. During the start-up the radial velocity in liquid phase increases to  $180 \text{ m/s}$  at the centerline while the pressure is building up at the exit of the nozzle. Farther from the centerline, the velocity decreases slightly; thus, the velocity reaches its maximum value at the centerline. On the other hand, at the liquid/gas interface ( $r \sim 100 \mu\text{m}$ ) the gas flow appears to experience vortical motion very close to the interface. The deviations seen on the graph at  $200 \mu\text{s}$  close to the interface explains the effects of these vortical structures. The sharp gradients of velocity profile observed near the interface are a result of the thin gas shear layer with thickness

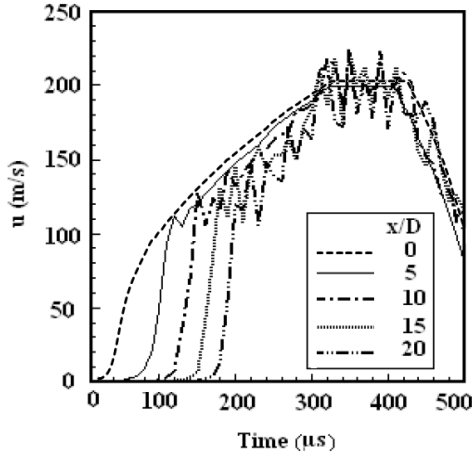


Figure 2: Jet centerline axial-velocity vs. time at different positions downstream of the orifice exit,  $\frac{\rho_g}{\rho_l} = 0.048$ ,  $\Delta p_{max} = 1.6$  MPa,  $Re = 1600$ ,  $We = 23000$ , and  $Fr = 17$ .

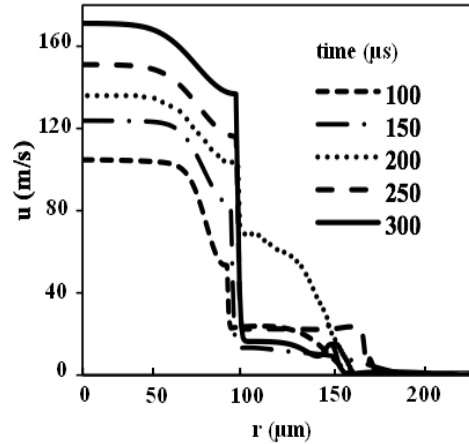


Figure 3: Velocity profile of the liquid jet and surrounding gas at  $x=1D$  at different instants of injection during start-up,  $\frac{\rho_g}{\rho_l} = 0.048$ ,  $\Delta p_{max} = 1.6$  MPa,  $Re = 1600$ ,  $We = 23000$ , and  $Fr = 17$ .

of the order of  $5-10 \mu\text{m}$ . Applying the continuity of both velocity and shear stress at the interface, we expect higher velocity gradient in the gas phase since its viscosity is much smaller than that of the liquid ( $\mu_g/\mu_l = 0.0068$  and  $\nu_g/\nu_l = 0.14$  for high density gas, i.e.  $\rho_g = 38 \text{ kg/m}^3$ ). Therefore, assuming the shear layer growth rate in the gas phase is associated with the viscous diffusion, we expect small-thickness shear layer in the gas phase since the kinematic viscosity of the gas is one order of magnitude smaller than that of the liquid. The nonlinear waves resulting from hydrodynamic instability form vortex structures that affect the shear layer near the interface. Protrusions (which are actually dynamic excursions of the interface) grow and wind from the interface, with small ligaments of fluid breaking from liquid jet. The protrusions appear to be associated with coherent vortex structures of the type envisioned by Abania and Reitz (12) and Ning *et al.* (3). The ligaments and drops observed in experiments are actually liquid conical sheets and fluid rings in our axisymmetric simulations. Thus, they have been used interchangeably within this text.

The numerical resolution must be sufficient to capture this vortex struc-

ture development since these vortices produce the fingers that break-up and form the spray. For a finger that, in three dimensions, has a location of minimum cross-sectional area in the liquid, capillary action can cause this neck to shrink and cause breaking. The presence of capillary stress in the model will allow this to happen. For a location in the liquid where local thinning brings two opposite interfaces close together without forming a neck, the disjoining pressure might become a factor; however, we have not included that physics in our analysis. This physics would lead to a local puncture of the liquid. The tearing of the liquid can be followed by deformations due to aerodynamic and capillary forces that enhance further break-up. Therefore, further three-dimensional computations perhaps with consideration of disjoining pressure seem necessary to investigate the formation of the droplets from the ligaments observed in the present axisymmetric simulation. The ligaments here are actually conical sheets and what is being observed as droplets are actually rings of fluid due to the axisymmetric nature of our numerical simulation; however, the effects of acceleration on the primary protrusions is the same for both axisymmetric and three-dimensional analysis. For a plane surface subject to a constant acceleration directing normal to that surface the temporal growth rate and the maximum amplified RT wavelengths has been predicted based on the linear instability theory (32). The same effects has been investigated for the co-flow jet (33) and liquid sheets experiments (34) that lead to the formation of ligaments and finally droplets.

The accelerating behavior of the liquid jet during the start-up is the main focus of this research. Figure 4 graphs the length of the jet as it is developing with time for Re number equal to 1600 and 2000 during the transient and steady-state period of injection. The jet length (furthest centerline position of the jet) increases with a positive acceleration for both Reynolds numbers. The higher Reynolds-number jet has more momentum relative to various drag effects; so, it penetrates farther and produces a longer jet at comparable instants of time. For the lower Reynolds number case this lack of momentum leads to a shorter liquid jet at different stages of injection. During the steady-state period of injection ( $300 \mu s < t < 400 \mu s$ ) the length of the jet is increasing with a constant velocity which is nearly the same for both Reynolds numbers. However, during the shut-down period, the length of the jet is increasing with a lower rate compared with the start-up and steady-state. The decelerating motion complies with the concave portion of the graph.

It is instructive to investigate the behavior of a point located on the centerline at an optional initial position downstream of the orifice that moves

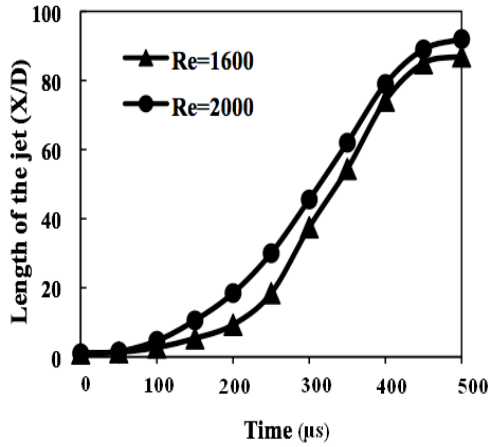


Figure 4: Length of the liquid jet vs. time during start-up, steady-state, and shut-down period for different Re numbers,  $\frac{\rho_g}{\rho_l} = 0.048$ ,  $\Delta p_{max} = 1.6$  MPa,  $We = 23000$ , and  $Fr = 17$ .

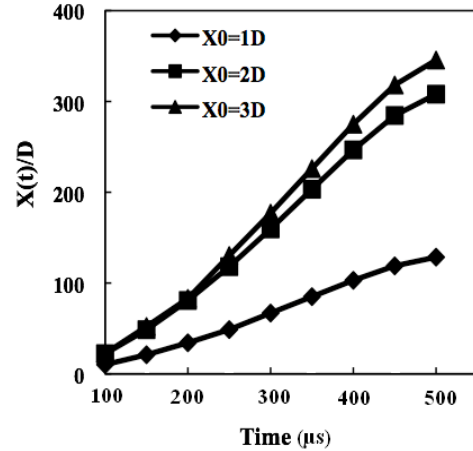


Figure 5: Axial position of a liquid point on the centerline moving from different initial positions vs. injection time,  $\frac{\rho_g}{\rho_l} = 0.048$ ,  $\Delta p_{max} = 1.6$  MPa,  $Re = 1600$ ,  $We = 23000$ , and  $Fr = 17$ .

with the liquid velocity at that point. The initial positions of the three different points selected for this analysis are 1, 2, and 3 diameters downstream of the orifice, respectively. The horizontal distance traveled by each of these points vs. injection time have been graphed in figure 5. Three different segments detected in these curves repeat the same trend described in figure 4 for start-up, steady-state, and shut-down period.

Further analysis of these graphs gives the magnitude of the acceleration and the constant velocity of the steady-state segment of the jet (see table 2.) According to this table, the acceleration of the liquid jet during start-up and shut-down is approximately  $10^4$  and  $10^5$  times greater than gravity, respectively. So, gravity is insignificant in these calculations. This high acceleration is consistent with the expectation for RT instability based on Viscous Potential Flow theory (20). In addition, points initially located at a further distance downstream of the orifice move with a greater acceleration during transient portions of the injection and also greater constant velocity during the steady-state period of injection. Table 2 gives the magnitude of the acceleration and the constant velocity of the steady-state segment of the

$X_0/D$	Acceleration $\times 10^5$ m/s <sup>2</sup>		Steady-State Velocity (m/s)
	Start-up	Shut-down	
1	1.68	-4.82	70
2	4.02	-11.81	170
3	4.61	-12.04	200

Table 2: Kinematics of the liquid particle motion downstream of the orifice,  $Re=1600$ ,  $We=23000$ .

jet.

Figure 6 illustrates the formation of a mushroom-shaped cap as the jet develops along the chamber while the pressure drops and the jet exit velocity increases during the first  $30 \mu s$  from the start of injection. The mushroom-shaped cap grows in volume and vortices at the interface roll back and entrain air into the rear side of the cap. This figure also illustrates the effects of liquid viscosity on the jet development for the same pressure difference at the orifice exit at the same instant of time. The viscosity of the liquid in (b) is 10 times that of (a). The discrepancies between the unstable structures at the liquid/gas interface on the cap shown in figure 6(a) and (b) are significant.

High  $Re$  number jet is associated with longer and thinner ligaments with RT wavelengths appearing at the rear side of the cap as the magnified window on the right hand side of the picture illustrates. In other words, the front of the jet decelerates due to the drag forces acting on it. So, the lighter fluid is then accelerating into the heavier fluid, which according to RT theory would be stabilizing on the front side of the jet cap and destabilizing on the rear side of the jet cap. However, due to the stabilizing effects of viscosity we did not detect RT waves at the back of the cap for case (b) at  $30 \mu s$ . However, as time elapses, longer RT wavelengths compared to case (a) sit at the back of the jet cap. For  $Re$  numbers greater than 1000, the separation of the flow from the nozzle at the upstream curved corner generates a recirculation zone that may extend throughout the orifice channel. This phenomenon known as hydraulic flip entrains air into the orifice and fills the recirculating zone. One way to avoid hydraulic flip is to increase the length of the orifice channel; the orifice channel for case (a) is twice that of (b). The effects of cavitation and flow recirculation on jet instability has been explained (26).

Figure 7(a) shows that the mushroom-shaped cap deforms after  $40 \mu s$

from the start of injection and well-known KH instabilities appear on the liquid/gas interface. This figure confirms the existence of the second type of instabilities at the back of the jet cap. These waves appear due to the RT instabilities. The reason behind this claim is that firstly, unlike the primary KH wavelengths, RT waves depend upon accelerations normal to the surface of the flow and have smaller wavelengths compared to the primary KH wavelengths. Secondly, RT wavelengths appear at the edges of the primary instabilities shortly after the formation of the KH instability at the interface. Therefore, RT instability can be considered as a secondary instability of the primary KH corrugation at the interface.

Mormottant and Villermaux (33) investigated the mechanisms responsible for the formation of corrugations, ligaments, and droplets at the interface of the liquid jets with a co-flow experiment. They claimed that the acceleration perpendicular to the to the passage of the travelling primary undulations is responsible for producing the secondary RT instability. In addition, RT instability occurs when the amplitudes of the primary waves is around its maximum. The large amplitude protrusions accelerated in the gas stream develop secondary RT instabilities at their edges. This configuration is very similar to what we observed numerically for the axisymmetric liquid jet. The sensitivity of the short-wave RT instabilities to the surface tension has also been investigated in Marmottant's experiment. They state that unlike the KH wavelength that depend on the shear instability at the interface, the RT wavelengths depend strongly on the surface tension. The effects of surface tension on jet instability for two instants of injection time have been shown in figure 8(a) and (b). The surface tension coefficient in (b) is 10 times that of (a); the  $Re$  number equals to 1600 for both cases. Clearly, by decreasing the surface tension, longer and thinner ligaments form and small wavelengths appear at the rear side of the jet cap at  $30 \mu s$  and strong KH and RT waves appear on the liquid/gas interface at  $80 \mu s$ . Thus, for the range of  $Re$  and  $We$  numbers that we are considering, we expect small-scale wavelengths and protrusions that become even smaller due to exposure to high accelerations normal to their interface, i.e., RT instability. The prediction of these small-scale wavelengths is of great importance.

According to Varga *et al.* (18), the scale of the primary mean droplet sizes during the atomization process are close to the most unstable RT wavelength. The most interesting unstable structures, especially the secondary instability occurs after the mushroom-shaped cap develops during the first  $30 \mu s$  after the start of injection. For lower  $Re$  numbers shown in figure 7(b), the RT

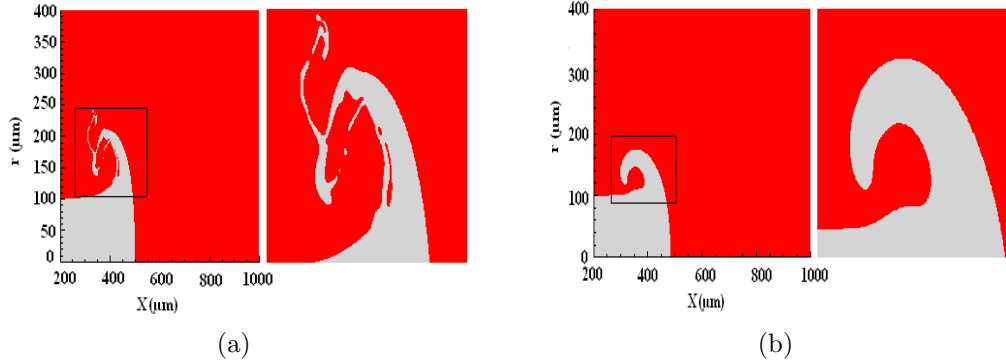


Figure 6: Jet development at  $30 \mu s$ ,  $\frac{\rho_g}{\rho_l} = 0.048$ ,  $\Delta p_{max} = 1.6 \text{ MPa}$  (a)  $Re = 16,000$ ,  $We = 230,000$ , and  $Fr = 17$  (b)  $Re = 1600$ ,  $We = 230,000$ , and  $Fr = 17$ .

wavelengths are significantly larger compared to case (a). This is consistent with the fact that viscosity has stabilizing effects for shorter wavelengths if surface tension is constant. Based on the potential flow analysis, the surface tension has stabilizing effects for high jet velocity and high  $Re$  numbers (20).

Figure 9 graphs the severe KH and RT instabilities at the interface and the size of these wavelengths 30 to  $100 \mu s$  after the start of injection for  $Re$  and  $We$  numbers equal to 16,000 and 230,000, respectively. Primarily, 30 to  $40 \mu m$  wavelengths appeared at  $30 \mu s$  after the start of injection turn into 10 to  $20 \mu m$  wavelengths at  $40 \mu s$  due to secondary instabilities. Simultaneously, as the liquid jet develops with time, the primary KH wavelengths increase to  $100 \mu m$  at  $50 \mu s$  and continue to increase up to  $300 \mu m$  at  $100 \mu s$  that is greater than the diameter of the orifice. The RT wavelengths associated with these longer KH waves also increase to  $30 \mu m$  at  $100 \mu s$  compared to 10 to  $20 \mu m$  wavelengths observed earlier. As mentioned before, the liquid jet builds momentum at the early stages of the injection while the pressure difference at the orifice increases. In addition, the drag forces acting on the liquid are also stronger at the beginning of injection. This corresponds to higher jet acceleration and high shear stress at the liquid/gas interface leading to small wavelength KH and RT instabilities. As the jet develops, the acceleration of the liquid jet and the drag forces decrease; thus, longer wavelengths appear at the interface.

Figure 10(a) depicts the jet development during the steady-state, i.e.,  $350 \mu s$  after the start of injection for  $Re$  and  $We$  numbers equal to 16,000

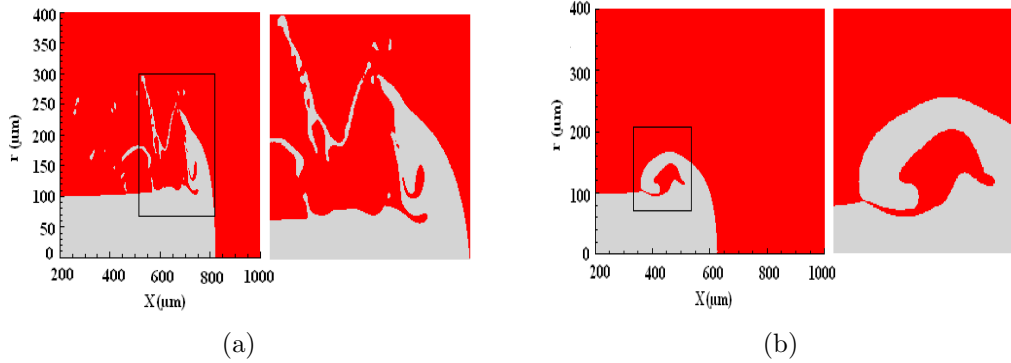


Figure 7: Jet development at  $40 \mu\text{s}$ ,  $\frac{\rho_g}{\rho_l} = 0.048$ ,  $\Delta p_{max} = 1.6 \text{ MPa}$  (a)  $Re = 16,000$ ,  $We = 230,000$ , and  $Fr = 17$  (b)  $Re = 1600$ ,  $We = 230,000$ , and  $Fr = 17$ .

and 23,000, respectively. The instantaneous interface is displayed and strong instabilities are seen along the edges and moving front of the jet. As the jet develops along the chamber the core width of the liquid jet increases and the ligaments that drawn out of the jet grow in the radial direction. The typical KH instabilities and RT wavelength can be detected with long wavelengths, i.e., greater than  $400 \mu\text{m}$  and  $70 \mu\text{m}$ , respectively, which are larger compared with the start-up.

As figure 10(b) graphs, the instabilities that were initiated prior to the beginning of shut-down have endured. However, these waves become longer downstream of the jet and persist for a longer time compared to start-up. The jet is continuing to be extended during the shut-down although the local flow rate is now decreasing with downstream distance implying that mass is accumulating in the forward part of the jet; that is, the jet core velocity is decreasing with downstream distance such that the jet front has a lower velocity than the orifice exit flow. On the other hand, during the shut-down transient the heavier liquid is decelerated into the lighter liquid. Thus, RT instability appears at the front part of the jet as shown on the magnified window in figure 10(b).

As was observed in figure 6(a) and 7(a) a few ligaments have detached from the liquid core as a characteristic of 2D axisymmetric simulations. This rupturing is not a characteristic of the break-up at later stages since these ligaments often continue to break-up by capillary instabilities producing a range of small-scale drops. The break-up of these ligaments is dependent

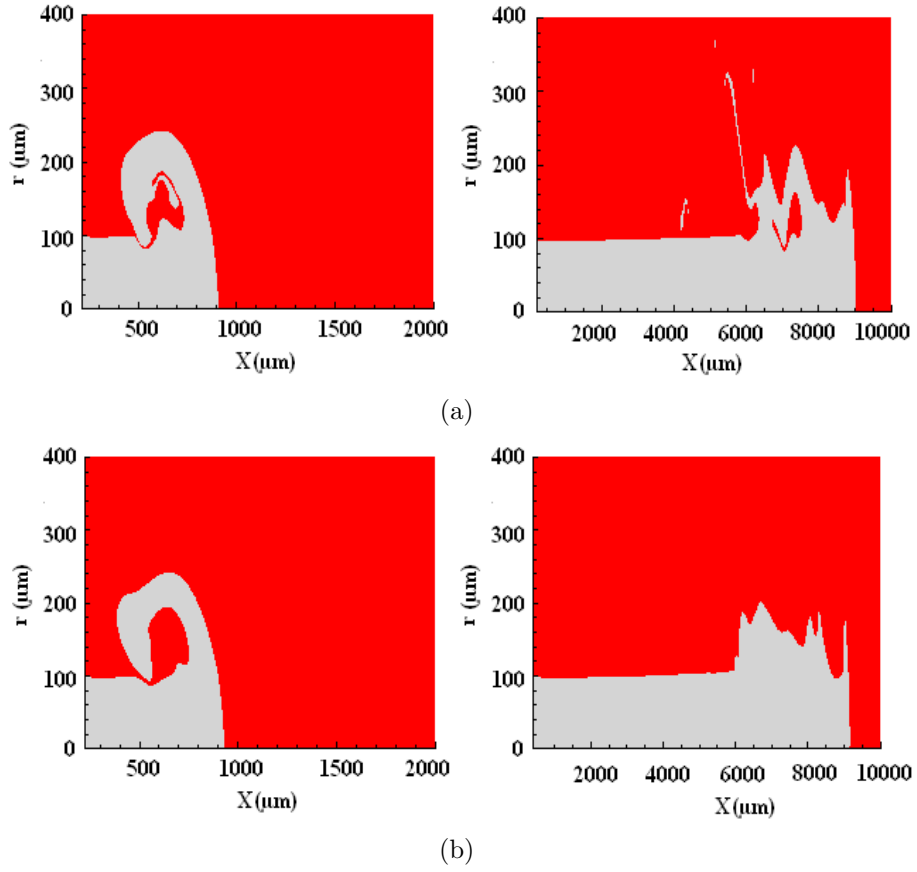
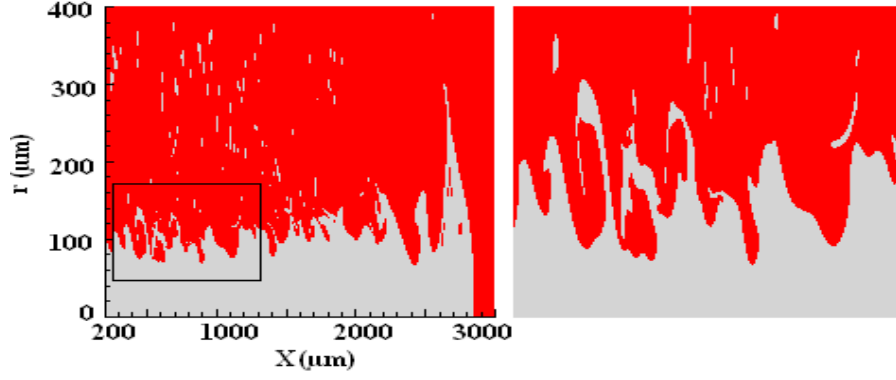
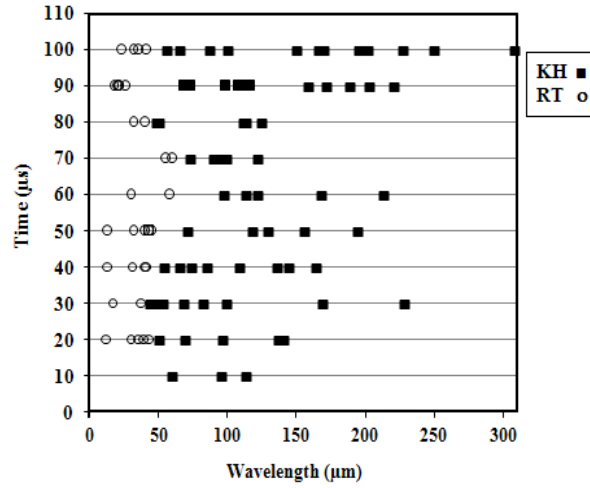


Figure 8: Jet development at  $30 \mu\text{s}$  (left) and  $40 \mu\text{s}$  (right),  $\frac{\rho_g}{\rho_l} = 0.048$ ,  $\Delta p_{max} = 1.6 \text{ MPa}$ ,  $Fr = 17$ , and  $Re = 1600$  (a)  $We = 230,000$  (b)  $We = 23,000$ .



(a)



(b)

Figure 9: (a) Unstable structures at the liquid interface during start-up at  $100 \mu\text{s}$  and magnified picture of the interface (b) KH and RT wavelength spectrum from the numerical simulation during start-up vs. time ( $\frac{\rho_g}{\rho_l} = 0.048$ ,  $\Delta p_{max} = 1.6 \text{ MPa}$ ,  $Re = 16,000$ ,  $We = 230,000$ , and  $Fr = 17$ .)

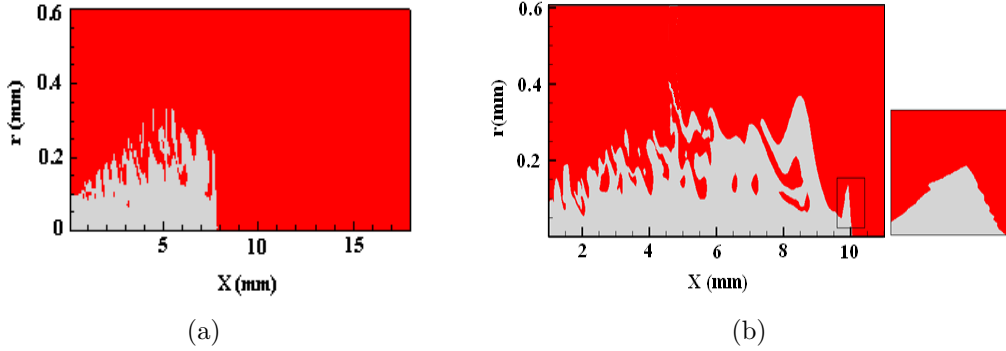


Figure 10: Simulated jet development,  $\frac{\rho_g}{\rho_l} = 0.048$ ,  $\Delta p_{max} = 1.6$  MPa,  $Re = 16,000$ ,  $We = 23,000$ ,  $Fr = 17$ , (a) steady-state at  $t = 350 \mu s$  (b) shut-down at  $t = 450 \mu s$ .

on the grid resolution. A coarse grid produces thicker ligaments and larger droplets when detached from the jet core. If we were considering secondary atomization models these larger droplets would turn into smaller droplets later in time. This dependence on the numerical grid resolution has been reported (16).

Figure 11 shows the effects of mesh sizes on the size of detached ligaments from the interface for mesh size equal to 0.5, 1, and 2  $\mu m$  at two instants of injection time, namely 30 and 50  $\mu s$  after the start of injection. It appears in all cases that most of the drops and ruptured segments of liquid are produced near the tip of the liquid jet due to large velocity differences between the liquid and the stationary gas. However, as the jet develops, more ligaments break-up from the interface further upstream from the jet head. These pictures show that a coarse grid produces thicker ligaments and larger droplets when detached from the jet core. Other than the size of detached ligaments, the first two cases (i.e., 0.5 and 1  $\mu m$ ) show similar behavior in terms of the jet velocity, jet penetration and interface instability; however the ligaments of the 2  $\mu m$ -case detach from the interface before they curl at the back of the jet head as was observed in the first two cases. In other words, the 2- $\mu m$  resolution seems insufficient to capture the jet penetration behavior during start-up. Therefore, the grid resolution on which the level set function has been solved coupled with Navier-Stokes equations dictates the break-up length and diameter of the ruptured segments of the liquid jet. The interface thickness based on which the liquid and gas properties have

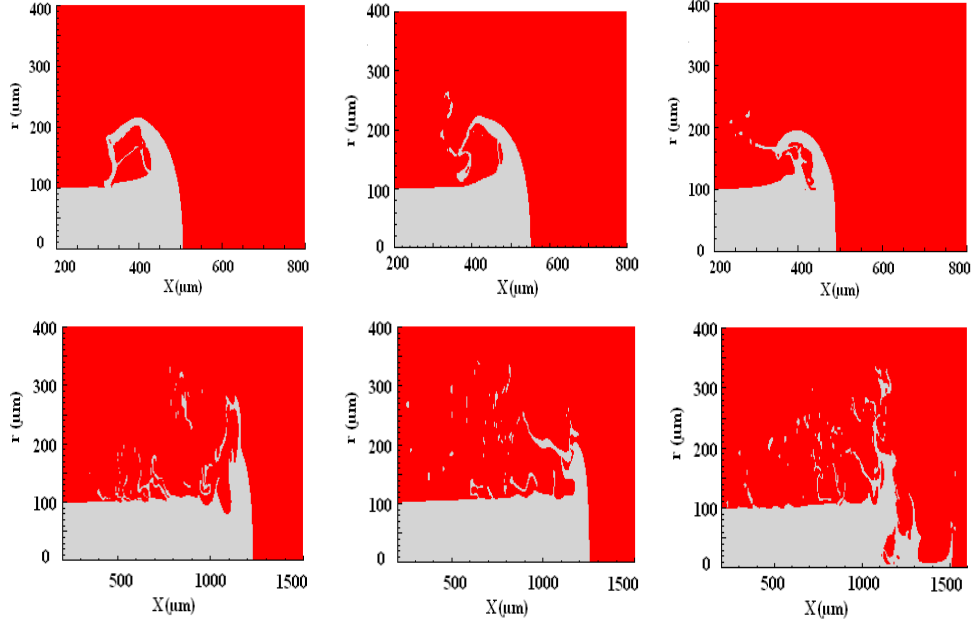


Figure 11: Impact of grid-resolution at  $30 \mu s$  (top) and  $50 \mu s$  (bottom),  $\frac{\rho_a}{\rho_l} = 0.048$ ,  $\Delta p_{max} = 1.6 \text{ MPa}$ ,  $Re = 16,000$ ,  $We = 23,000$ ,  $Fr = 17$ :  $\Delta x = \Delta r = 0.5 \mu m$  (left),  $\Delta x = \Delta r = 1 \mu m$  (center),  $\Delta x = \Delta r = 2 \mu m$  (right).

been defined equals to three mesh sizes, i.e.,  $3 \mu m$  for  $1 \mu m$  grid resolution. So, our results are consistent with accepted findings in the spray atomization field. The hydrodynamic stabilities can be predicted well by computation. However, the prediction of the break-off of ligaments and droplets will have quantitative inaccuracies.

The independency of the solution on the size of the computational domain has been investigated. The difference in axial velocity of liquid points located on the axis of symmetry close to the jet tip (e.g. 2D downstream of the orifice at  $30 \mu s$  after the start of injection) for a computational domain twice the length and height, i.e., 4D and 40D, is less than 0.003%. The number of mesh points in both axial and radial directions is also doubled keeping the mesh size  $\Delta x = \Delta r = 1 \mu m$ . The unstable structures at the interface for these two computational domains demonstrated in figure 12 show similarities in terms of wavelengths and shape of ligaments. Here, the total mass of liquid in the

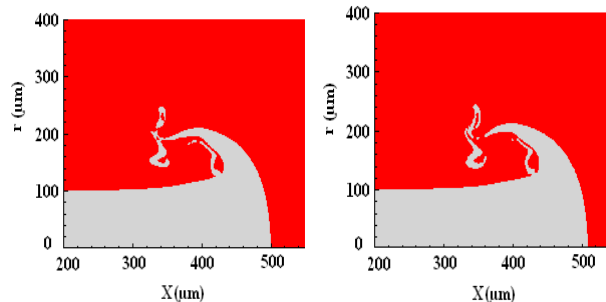


Figure 12: Impact of the size of computational domain, 20D length and 2D height (left), 40D length and 4D height (right) at  $30 \mu s$  after the start of injection,  $\Delta x = \Delta r = 1 \mu m$ ,  $Re = 16,000$ ,  $We = 230,000$ , and  $Fr = 17$ .

computational domain is prescribed to vary with time. So, we have used the Liquid-Segment model of section 4 to evaluate the reliability of our level-set technique. For that model, constant liquid mass with time is prescribed.

The qualitative characteristics of the unstable interface during start-up that were discussed before agree well with the experimental observation of (10). They detected periodic structures, voids, and the appearance of ligaments, some of which appear to roll-up and entrain air during the process that is consistent with the unstable structures that we obtained numerically. In their experiment, the transient liquid jet is injected through an orifice with  $155 \mu m$  diameter into air at atmospheric pressure at 300 K. The density ratio,  $Re$  number, and  $We$  number are 0.0011, 16000, and 7.6e5, respectively. The maximum jet velocity reaches 370 m/s during the steady-state period.

The numerical simulations have been adapted to this flow configuration in order to investigate the quantitative agreement between them. The range of unstable wavelengths from the numerical simulation compared with the experiment has been shown in figure 13. The numerical results demonstrate both KH and RT wavelengths at different instants of injection time and the shaded areas show the length of the experimentally observed periodic structures. The numerical results predict shorter wavelengths compared to experiments. The RT wavelengths between 10 to  $70 \mu m$  and KH wavelengths between 90 to  $130 \mu m$  have not been reported in the experiment, probably due the difficulties in detecting the small-scale instabilities close to the nozzle and the limited spatial resolution of the imaging techniques. However, the longer unstable wavelengths remain in the predicted range of experiments,

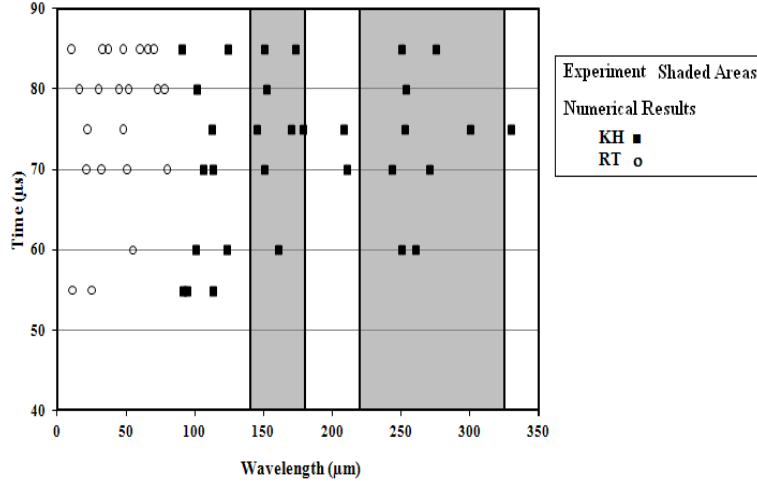


Figure 13: Wavelength spectrum from the numerical simulation during start-up vs. injection time for both KH and RT instabilities, compared with the experiment of (10): gray areas.

i.e., 140-180 and 220-350  $\mu\text{m}$ .

As mentioned before, the early stage of start-up is of great importance. Very small-scale secondary instabilities at the rear side of the jet cap need very good resolution to be captured in numerical simulation. Therefore, we treat the early start-up phenomena using the full transient jet model discussed above. However, due to the drag forces acting on the bulk accumulated liquid on the jet cap, the jet centerline velocity decreases drastically in the axial direction. Figure 14 describes the effects of  $Re$  number on the deceleration of the liquid jet during the start-up period of injection, i.e., 100  $\mu\text{s}$  after the start of injection. Based on the results shown in figure 14 for higher  $Re$  numbers, the jet tip moves approximately at the speed equal to the jet exit velocity and the effects of drag forces are not dominant in the downstream direction. In other words, we can assume that the liquid points on the centerline of the jet have the same acceleration as the jet injection at the nozzle exit. (14) assumed that the acceleration of the jet exit is immediately translated to all parcels in the liquid core to capture the initial penetration phase of the transient jet. This essentially portrays any element of mass as a ballistic slug of liquid following a constant velocity with time; i.e., the Lagrangian time derivative is zero although velocity spatially varies in the

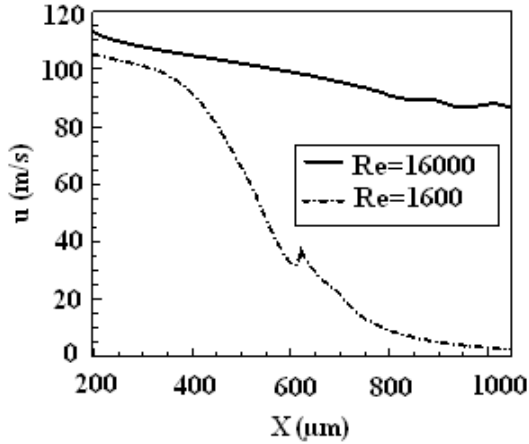


Figure 14: Effects of jet  $Re$  number on ambient gas and centerline velocity with downstream distance at  $100 \mu s$ ,  $\frac{\rho_g}{\rho_l} = 0.048$ ,  $\Delta p_{max} = 1.6$  MPa,  $We = 23,000$ , and  $Fr = 17$ .

downstream direction. Thus, for larger  $Re$  numbers we can examine stream-wise segments of the jet, treating these segments as ballistic slugs coming from the orifice instead of simulating the full jet. The Liquid-Segment model for simulating further instabilities at the jet interface after the jet cap has deformed due to severe instabilities will be discussed in section 4.

### 3.2 Instability Analysis

There are four physical phenomena which contribute to the hydrodynamic instability: (1) acceleration normal to the interface, i.e., Rayleigh-Taylor (RT) instability; (2) inertial difference across the shear layer at the jet interface, i.e., Kelvin-Helmholtz instability; (3) capillary effects; and (4) viscous effects. The magnitude of the growth rate increases with increasing wave number (decreasing wavelength); however, surface tension has stabilizing effects on shorter wavelengths and decreases the growth rate. These four effects are ordered above so that, in the dispersion relation for the growth rate obtained for viscous potential flow discussed by Joseph *et al.* (20), the four related terms appear proportional to wave number to the first, second, third, and fourth power, respectively. So, viscous effects dominate at very short wavelengths while gravity effects dominate at very long wavelengths. If an acceleration much larger than gravitational acceleration is applied, short wavelength can

be experienced; this is the situation in our transient jet. The acceleration term is destabilizing (stabilizing) when the heavier (lighter) fluid accelerates into the lighter (heavier) fluid. The Kelvin-Helmholtz instability is a type of shear instability of the interface of two fluids with a velocity discontinuity with no shear layer. In reality, two separate boundary layers with different thicknesses form at the interface and both velocity and the shear stress are continuous. The effects of this finite-size shear layer on the instability of two parallel streams with same densities was first investigated by Rayleigh (35). Marmottant and Villiermaux (33) has analysed the transition between the pure Kelvin-Helmholtz and Rayleigh instability for two parallel streams and proposes a criterion based on the liquid density ratios, vorticity or shear layer thickness and the velocity of the less dense fluid, and surface tension. In satisfying that limit, the Rayleigh instability overcomes the pure Kelvin-Helmholtz instability. As discussed earlier the shear layer thickness in our numerical simulation is small; therefore, the shear instability lies within the Rayleigh limit.

The Kelvin-Helmholtz effect is always de-stabilizing while the viscous effect is always stabilizing. The capillary effect is always stabilizing when the surface radius of curvature is sufficiently large; however, it can be important in the three-dimensional pinch-off of smaller ligaments from the surface. Another mechanism that can play a role in the final pinch-off of ligaments is disjoining pressure. Depending upon the balance between these terms, the jet will be stable or unstable.

The Rayleigh-Taylor instability is a result of the accelerations perpendicular to the liquid interface that has been the subject of the primary Kelvin-Helmholtz instability. When the acceleration is directed towards the liquid (dense fluid) the interface becomes unstable (36; 37). RT instability has been analyzed (20) as a viscous potential flow. In their analysis Navier-Stokes equations are reduced to an identity provided that the pressure is given by Bernoulli's equation. Liquid acceleration points down against the direction of height increasing. It is assumed that the heavy fluid is above the light fluid, or that the light fluid is accelerated into the heavy fluid above. The following dispersion relation depicts the relation between temporal growth rate and wave number;

$$\omega = -k^2 \frac{\mu_l + \mu_g}{\rho_l + \rho_g} \pm \left[ \frac{\rho_l \rho_g k^2 (u_g - u_l)^2}{(\rho_l + \rho_g)^2} - k \frac{\rho_l - \rho_g}{\rho_l + \rho_g} g - \frac{k^3 \sigma}{\rho_l + \rho_g} + k^4 \left( \frac{\mu_l + \mu_g}{\rho_l + \rho_g} \right)^2 \right]^{1/2} \quad (5)$$

where  $\omega$  is the temporal growth rate,  $\mu_l$ ,  $\mu_g$ ,  $\rho_l$ , and  $\rho_g$  are the viscosity and density and the indices  $l$  and  $g$  refer to liquid and gas, respectively.  $\sigma$  is the surface tension coefficient,  $k$  is the wave number,  $g$  is the gravitational acceleration that can be replaced by the acceleration of the light fluid into the heavy liquid since this acceleration is considerably greater than gravitational acceleration (about  $10^5 g$ ) as discussed in the previous section. If the quantity under the root is negative, then the real part is negative and the interface is stable.

Varga *et al.* (18) developed a model for the initial break-up of an inviscid liquid jet by a high-speed coaxial gas stream based on the classic linear stability analysis by (32), including the effects of surface tension. The RT instability dispersion relation and wavelength has been predicted as follows:

$$\omega = \left[ \frac{k(\rho_l - \rho_g)a - k^3 \sigma}{\rho_l + \rho_g} \right]^{1/2} ; \quad \lambda_{RT} = 2\pi \sqrt{\frac{3\sigma}{\rho_l a}} \quad (6)$$

where  $\lambda_{RT}$  is the RT instability wavelength and  $a$  is the acceleration.

Figure 15 shows a plot of the real part of the growth rate versus wavelength following Joseph *et al.* (20) using the same parameters mentioned in table 1 and acceleration,  $Re$ , and  $We$  numbers equal to 800,000  $m/s^2$ , 1600 and 23000 respectively. Positive values indicate the instability region while negative values imply stability. Clearly, at sub-micron wavelengths, where viscosity and capillary effects dominate, we find stable behavior. The dispersion relation reflected in 5 accounts for both Kelvin-Helmholtz and Rayleigh-Taylor instabilities. This figure clearly shows that instabilities are expected in the wavelength range that are found in our simulations, i.e.,  $O(10^{-6} - 10^{-3} \text{ m})$ . As shown for our sub-millimeter, super-micron wavelength range of interest, unlike the liquid acceleration viscosity and surface tension are very important.

The liquid jet is accelerating through the orifice during start-up. In addition, liquid protrusions are exposed to an even higher acceleration normal to their interface. This normal acceleration causes the secondary RT instability at their edges. the crests of the primary instabilities moves in the streamwise

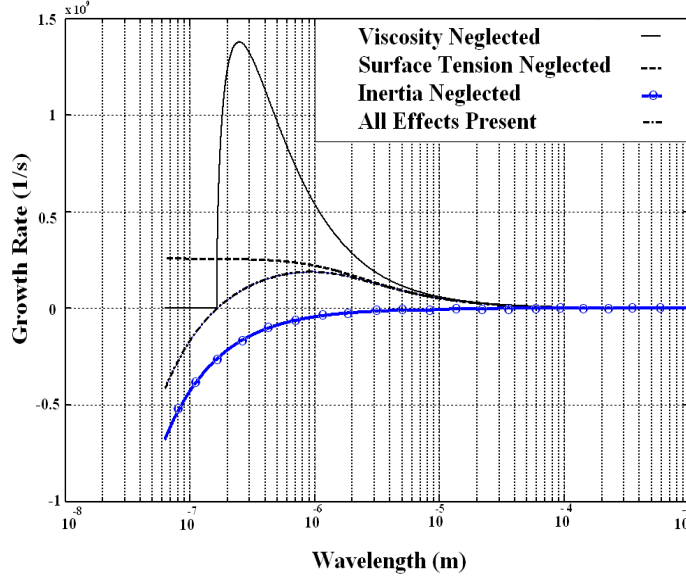


Figure 15: Real part of the linear growth rate as a function of wavelength based on VPF instability analysis (20).

direction. We have measured the change of this streamwise velocity of about 10 of each of these crests every 1 microsecond for about 60 microseconds after the start of injection. This time period has been used since the liquid jet is experiencing the highest acceleration during this period that is associated with more complicated unstable structures on the liquid jet. The local acceleration normal to the back of the jet cap is denoted by  $(a_n)$  and is of the order of  $10^6$ - $10^7$   $\text{m/s}^2$  compared to the liquid jet injection acceleration ( $10^5$ - $10^6$   $\text{m/s}^2$ ) discussed in table 2. The local acceleration  $(a_n)$ , the RT wavelengths, the thickness of the ligaments appeared at the rear side of the jet cap and on the interface during the first 60  $\mu\text{s}$  from the start of injection shown in figure 9 for  $Re$  and  $We$  equal to 16,000, 230,000 for a few selected ligaments and the local RT instability have been gathered in table 3. The last column of this table illustrates the theoretical RT wavelength as in 6 that has been extensively used in many publications as a mean to compare numerical simulations with experimental observations. Comparing our measurements with this theory shows a reasonable agreement. The discrepancies stem from the fact that, as mentioned earlier, this formula does not take into account the liquid viscosity that has stabilizing effects for shorter wavelengths. Therefore,

$t$	Thickness	$a_n$	Computed $\lambda_{RT}$	$\lambda_{RT} = 2\pi\sqrt{\frac{3\sigma}{\rho a_n}}$
$\mu s$	$\mu m$	$m/s^2$	$\mu m$	$\mu m$
26	11	8.4e6	27	21
36	12	2.3e7	14	13
55	35	2.7e6	40	38

Table 3: RT wavelengths compared with theory for full jet.

the measured RT wavelength is slightly larger compared to the theory.

Discrete Fourier Transform (DFT) of the interface of the jet 250  $\mu s$  after the start of injection is illustrated in figure 16. The peaks in the diagram correspond to the range of wavelengths captured at the interface which is greater than 100  $\mu m$  and smaller than 1600  $\mu m$  at that instant of injection. Further DFT analysis for the steady-state and shut-down periods not shown in this picture reveals the fact that shorter wavelengths appear during the start-up at the interface; as we approach the steady-state period of injection these short waves grow in length. The decelerating motion of the liquid during the shut-down segment of injection is associated with shorter wavelengths compared with the steady-state period. Averaging the results obtained for the total injection duration, i.e., 500  $\mu s$ , shows that the wavelengths characterized by this analysis are predominantly in the range from 10 to 1200  $\mu m$ . This result indicates the dimensions of the expected ligaments and droplets in the initial break-up of the jet and magnifies the fact that detecting the small waves during start-up and shut-down requires a good resolution in CFD calculations.

## 4 Liquid-Segment Model

The full jet instability as discussed earlier originates at a certain point and develops in space, in the direction of mean velocity, i.e., spatial instability. Numerical modeling of the spatial problem requires much longer computational domains to allow the spatial development of the flow. The jet instability problem simulated in the laboratory frame is now transferred to a new accelerating coordinate system consistent with the acceleration of the liquid on the centerline obtained in full transient jet simulation. The gas acceler-

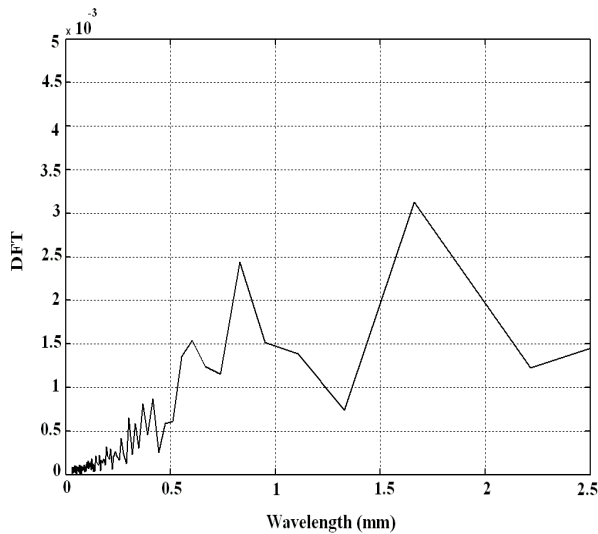


Figure 16: Fourier analysis of the interface during start-up at  $250 \mu s$  after the start of injection,  $Re = 1600$ ,  $We = 23000$ ,  $Fr = 17$ .

ates over the initially stagnant liquid and the generated instabilities at the interface will develop temporally. Since the temporal instability dominates in this model most comparisons reported here especially, the frequency and amplification rate of the instabilities are mainly qualitative. However, as will be illustrated the KH and RT wavelengths will stay in the same range as full transient jet.

We consider two points initially located at  $0.65D$  and  $0.85D$  on the center-line of the full jet and track these points during the start-up period, i.e.,  $300 \mu s$  and plot the axial velocity vs. time as shown in figure 17. As the graph shows, for the first  $60 \mu s$  associated with the formation of the mushroom-shaped cap, the acceleration increases up to  $10^6 \text{ m/s}^2$ . The acceleration of the liquid points remains approximately constant after about  $75 \mu s$  for both liquid points. The average acceleration for these two cases is about  $800,000 \text{ m/s}^2$ . We use this value of acceleration in the Navier-stokes equation shown in 4.

A small segment of the jet, e.g.,  $1 \text{ mm}$  with a  $200\text{-micron}$  radius surrounded by air at  $30 \text{ atm}$  is considered. The liquid is initially quiescent while the gas blows over the liquid from right to left. The gas initial velocity is consistent with the maximum velocity of the jet in the laboratory frame when its penetration length is  $1 \text{ mm}$ . The computational domain and boundary

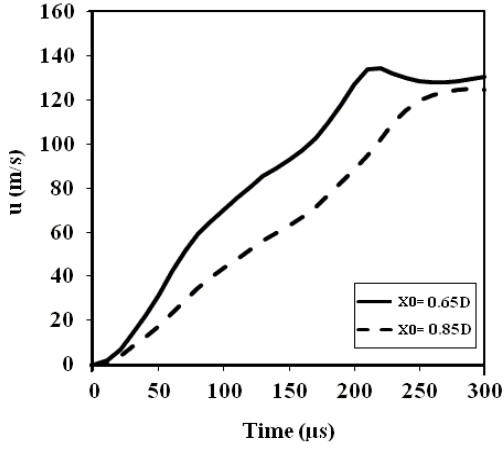


Figure 17: The axial velocity on the centerline of the full jet vs. injection time for two starting points,  $Re = 16,000$ ,  $We = 230,000$ ,  $Fr = 17$ .

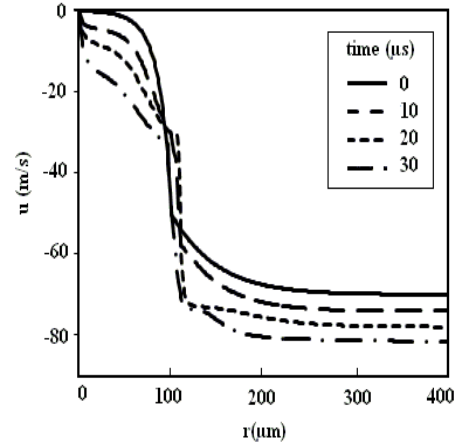


Figure 18: Liquid/gas velocity profile vs. radial direction for liquid-segment at different instants of time during start-up,  $Re = 16,000$ ,  $We = 230,000$ ,  $Fr = 17$ .

conditions are described in section 2. The fluid properties are based on the initial velocity profile consists of a small thickness boundary layer for the liquid varying between zero to 50 m/s along 100-micron orifice radius combined with a large thickness boundary layer for the gas varying between 50 to 70 m/s along 300  $\mu\text{m}$  in radial direction. Initial disturbances with 100  $\mu\text{m}$  wavelength have been applied on the liquid/gas interface in observation of the effects of instabilities due to nozzle cavitation during injection.

The velocity profile of both phases along the radial direction is shown in figure 18 at different instants of time. The velocity of the liquid and gas increases with time consistent with the constant acceleration of the frame of reference. As time elapses, oscillations appear at the velocity profile due to the surface instability and formation of liquid protrusions and vortical structures associated with rolled-up ligaments.

Figure 19 illustrates the development of the unstable wavelengths at the liquid/gas interface at two instants of time. The primary KH waves with wavelengths of 100-200  $\mu\text{m}$  travel to upstream relative to the liquid (left) while their amplitude increases and long ligaments (fingers) are drawn out of liquid. These ligaments turn and roll-up in the flow direction (right to left).

At the same time, they turn into a very thin film with a blob of liquid at the end. This phenomenon has been reported (1) for droplets accelerated by a constant force in a quiescent environment for large accelerations. In addition to the acceleration of the frame of reference, these ligaments are exposed to very high local accelerations normal to their interface that make them a good prey for small-scale RT instabilities (10-50  $\mu\text{m}$ ), these secondary instabilities appear at the edge of the ligaments formed by the primary KH instabilities at the interface.

Figure 20 illustrates the instabilities due to an acceleration which is two times that of figure 19 at 15 and 30  $\mu\text{s}$  after the start of injection while other parameters, i.e.,  $Re$ , and  $We$  numbers, remain constant. Increasing the acceleration of the frame of reference leads to the formation of longer and thinner ligaments with smaller RT wavelengths on their crests at comparable instants of time. It is instructive to investigate the effects of surface tension on jet instability. According to the viscous potential flow dispersion relation (21) at sub-millimeter, super-micron wavelength range of interest, unlike the liquid acceleration viscosity and surface tension are very important. Surface tension has stabilizing effects for smaller wavelengths; thus, at higher  $We$  numbers we expect smaller wavelengths. A comparison between figures 20 and 21 depicts that at a comparable instant of time after the start of injection smaller waves and thinner ligaments appear at the liquid/gas interface for higher  $We$  number with constant acceleration,  $Re$ , and  $Fr$  number.

We have performed a similarity simulation for a segment twice in length compared to the cases shown so far, i.e., 1 mm. The non-dimensional parameters namely, density ratio  $\frac{\rho_g}{\rho_l}$ , viscosity ratio  $\frac{\mu_g}{\mu_l}$ ,  $Re = \frac{\rho_l \bar{u} D}{\mu_l}$ ,  $We = \frac{\rho_l \bar{u}^2 D}{\sigma}$ ,  $Fr = \frac{\bar{u}}{\sqrt{aD}}$ , and non-dimensional time  $t^* = t \sqrt{\frac{a}{D}}$  should remain constant. For this purpose liquid and gas viscosity, surface tension coefficient, and orifice diameter has to be twice those values used for 1-mm segment. However, the acceleration is half of the shorter length segment to keep the  $Fr$  number constant. Furthermore, the mesh size and time step are twice that of the shorter length segment since the liquid viscosity has twice the value of the shorter length segment while the density ratio remains unchanged.

We expect wavelengths and ligament thicknesses to be twice that of the 1 mm-liquid segment applying the above mentioned parameters. Figure 22 demonstrates the discrepancies between the interface instabilities for 1-mm and 2 mm-segment at  $t^*=1.89$  for  $Re$ ,  $We$ , and  $Fr$  numbers equal to 16,000, 230,000, and 17, respectively. The thicknesses of the blobs at the tip of the

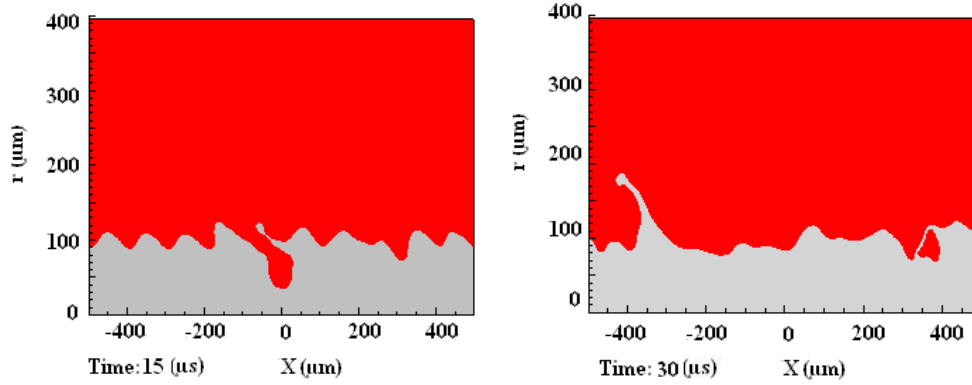


Figure 19: Instabilities at the liquid/gas interface for liquid-segment model at two instants of time:  $t = 15 \mu s$  (left) and  $t = 30 \mu s$  (right),  $Re = 16,000$ ,  $We = 23,000$ ,  $Fr = 17$ ,  $a = 400,000 \text{ m/s}^2$ .

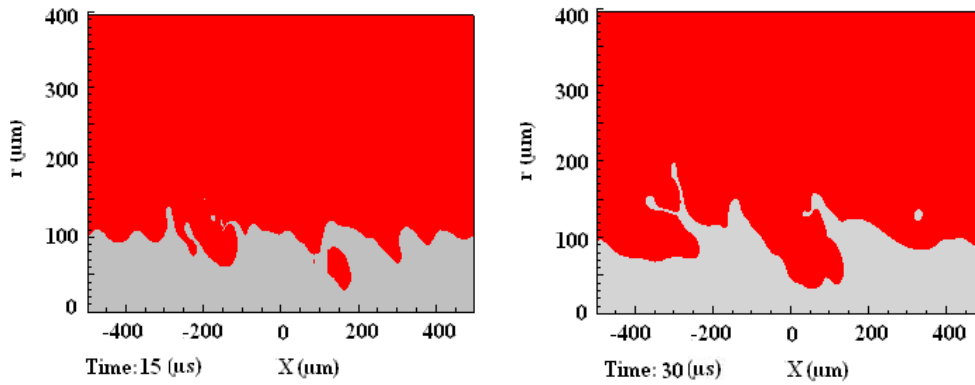


Figure 20: Instabilities at the liquid/gas interface for liquid-segment model at two instants of time:  $t = 15 \mu s$  (left) and  $t = 30 \mu s$  (right),  $Re = 16,000$ ,  $We = 23,000$ ,  $Fr = 12$ ,  $a = 800,000 \text{ m/s}^2$ .

ligaments indicated in the boxes, wavelengths appeared at the interface, and the amplitudes of these waves for 2 mm-segment are approximately twice that of the 1 mm-segment. The discrepancies are at most  $2 \mu\text{m}$ ; that is smaller than the interface thickness, i.e.,  $3 \mu\text{m}$  (3 mesh size) for 1 mm-segment comparable to  $6 \mu\text{m}$  for the 2 mm-segment. The thicknesses of these blobs are of great significance since the droplet sizes that will eventually detach from the ligaments probably have comparable sizes.

One of the concerns in applying the level set method for interface tracking is to check the conservation of mass; especially, when the ligaments become as small as the grid size leading to their detachment from the liquid core. Re-initialization technique used in this work (38) improves the mass conservation of the level set method. These methods known to be effective in maintaining the level set as a signed distance function for capturing more accurate interface curvature. We expect constant liquid volume in the liquid-segment model during the injection period as the periodic boundary conditions on the right and left boundaries of the computational domain implies. However, there are two factors affecting the liquid volume: firstly, the level set method deficiency in mass conservation, and secondly, the detachment of the liquid particles from the liquid jet body as discussed earlier. This issue has been investigated in figure 23. The liquid volume change with respect to the initial state during start-up changes from 0 to 0.7% after  $100 \mu\text{s}$  after the start of computation for a three-micron interface thickness keeping mesh spacing constant ( $1 \mu\text{m}$ ). The sudden jumps in the graph corresponds to the local tearing of the liquid at the edge of the liquid fingers which in turn depends on the computational grid size. Decreasing the level set interface thickness leads to a sharper change in fluid properties between the two-phases and locally thinner ligaments that detach easier from the liquid jet compared with a three-micron interface thickness. Therefore, the liquid volume change is higher for smaller interface thickness as figure 23 demonstrates.

The range of KH and RT wavelengths at the liquid/gas interface for the liquid-segment is shown in figure 24 for 10 to  $80 \mu\text{s}$  after the start of simulation for the liquid segment of length 1 mm with  $Re$ ,  $We$ , and  $Fr$  numbers equal to 16,000, 230,000, and 17, respectively. Initially, KH waves in the range of  $70\text{-}120 \mu\text{m}$  appear at the interface. Then, the wavelengths range extends due to secondary instability resulting from the acceleration of the gas blowing over the crests of these waves. The smallest wavelengths on the spectrum designate the RT wavelengths and the longer wavelengths indicate the KH instability. We detect waves as small as  $10 \mu\text{m}$  at  $20 \mu\text{s}$ , consis-

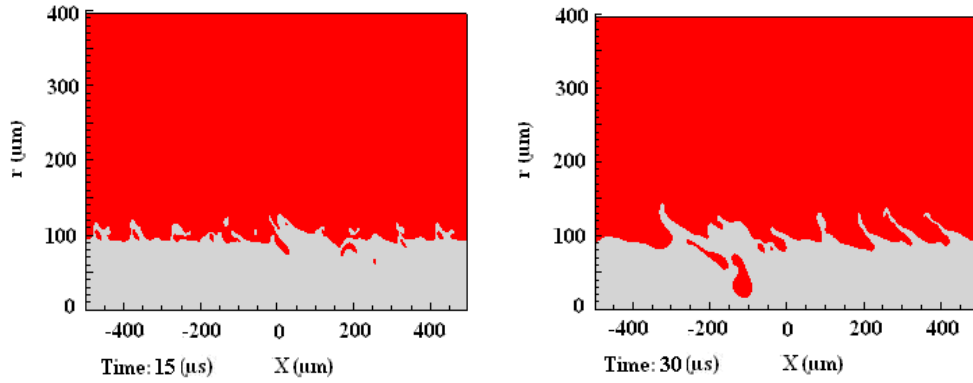


Figure 21: Instabilities at the liquid/gas interface for liquid-segment model at two instants of time:  $t = 15 \mu s$  (left) and  $t = 30 \mu s$  (right),  $Re = 16,000$ ,  $We = 230,000$ ,  $Fr = 12$ ,  $a = 800,000 \text{ m/s}^2$ .

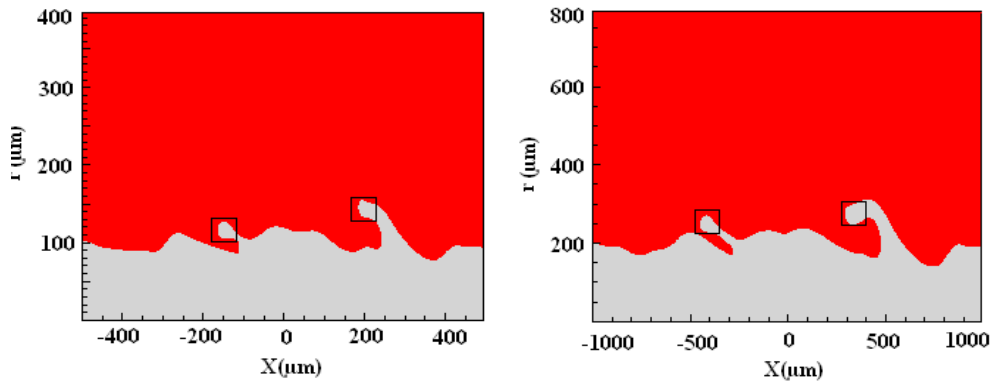


Figure 22: Similarity simulation for 1 mm-segment (left) and 2 mm-segment (right) at  $t^* = 1.89$ ,  $Re = 16,000$ ,  $We = 230,000$ ,  $Fr = 17$ .

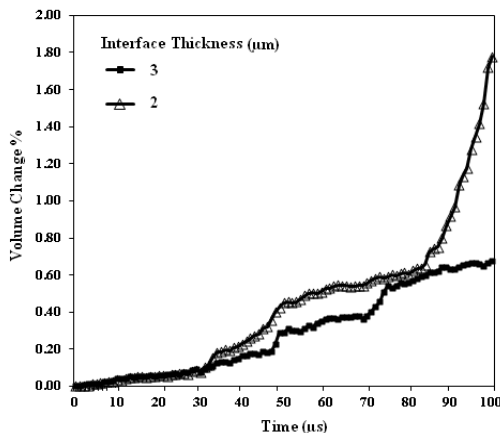


Figure 23: Effects of interface thickness used in level set method on liquid volume change with respect to the initial state in the liquid-segment during start-up,  $\frac{\rho_g}{\rho_l} = 0.048$ ,  $\Delta p_{max} = 1.6$  MPa,  $Re = 16,000$ ,  $We = 23,000$ ,  $Fr = 17$ .

tent with the full jet simulation shown in figure 9. It should be noted that full transient jet and liquid-segment cannot be exactly matched at a specific computational time due to the different nature of the analysis, i.e., spatial instability for full jet vs. temporal instability for liquid-segment. However, the liquid-segment qualitatively agrees with the full jet and predicts the same range of wavelengths observed in full jet simulations. For example, the primary KH waves become longer and the RT waves associated with them also increase in length as time elapses. This trend continues until the largest KH wave approach  $300 \mu\text{m}$  and RT waves grow to about  $35 \mu\text{m}$ . Once again, we can deduce that the effects of acceleration are mainly on the secondary instability. Consequently, the RT instability on the liquid jet should be studied together with KH instability which in turn is strongly dependent on the viscosity, density ratios, and the inertia of the two phases.

As mentioned earlier, the liquid-segment model is useful for the time that the instabilities appear at the interface as well as the mushroom-shaped cap and KH waves start to form at the interface, i.e.,  $60 \mu\text{s}$  after the start of injection. Therefore, the wavelengths observed at  $10 \mu\text{s}$  for the liquid-segment model is comparable to  $70 \mu\text{s}$  in the full transient jet analysis.

Different ligaments at the interface have been considered and their lengths, thicknesses, and the RT wavelengths at their edge have been measured as dis-

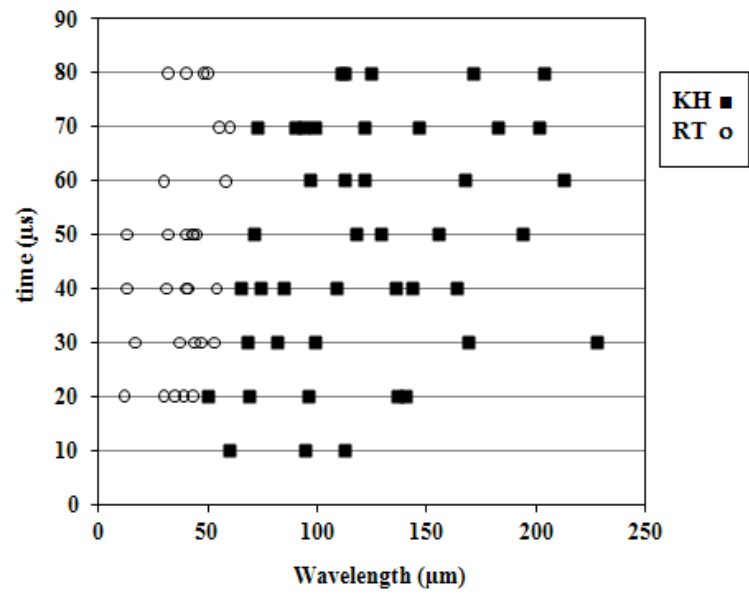


Figure 24: KH and RT wavelength spectrum during start-up vs. time for the liquid-segment numerical simulation ( $Re = 16,000$ ,  $We = 230,000$ ,  $Fr = 17$ .)

$t$	Thickness	$a_n$	Computed $\lambda_{RT}$	$\lambda_{RT} = 2\pi\sqrt{\frac{3\sigma}{\rho_l a_n}}$
$\mu s$	$\mu m$	$m/s^2$	$\mu m$	$\mu m$
17	8	2.35e6	43	38
18	12	2.04e6	45	41
19	11	4.07e6	36	29

Table 4: RT wavelengths compared with theory for liquid-segment.

cussed for full transient jet (see table 4.) The measured results show a good agreement with predicted RT wavelengths as described for full transient jet simulations. The discrepancies likely stem from the fact that the classical formulation neglects the effects of viscosity and nonlinearity of the problem.

Based upon the useful information obtained from the axisymmetric liquid-segment method, we expect that time-dependent, three-dimensional CFD combined with level-set method can be used for liquid-segment in the future to produce useful data relevant to the full jet situation. Development of the data from the liquid-segment simulation should produce a valid less-computationally-intensive than full jet analysis predictive three-dimensional model for initial droplet size and velocity distributions where very high computational resolution is necessary.

## 5 Conclusions

The behavior of the liquid jet injected into air at 30 atm has been simulated during start-up, steady-state, and shut-down. Use has been made of an unsteady axisymmetric code with a finite-volume solver of the Navier-Stokes equations for liquid streams and adjacent gas, a boundary-fitted-gridding scheme, and a level-set method for liquid/gas interface tracking.

The development of the transient jet into the gas involves strong instabilities along the edges and moving front of the transient jet. The simulation of the full jet depicts that, for lower Reynolds numbers, the starting liquid jet forms a cap which grows in volume as it moves downstream and decelerates along the gas chamber. However, for higher Reynolds numbers the mushroom-shaped cap deforms drastically within a few microseconds after the start of injection and KH and RT instabilities develop on the liquid/gas

interface. The simulations show that the primary KH wavelengths are on the order of 100-300  $\mu\text{m}$ . As the waves convected downstream, their amplitude increases and long ligaments are drawn out of the liquid. These ligaments further roll back and entrain air during the process, forming significant vortex structures. This behavior of the jet during transients is in good agreement with experimental observations of the transient liquid jet.

At high  $Re$  and  $We$  numbers, small-scale wavelengths and protrusions become even smaller due to exposure to high accelerations normal to their interface. This leads to small-scale RT waves at the edge of the ligaments. The normal acceleration on the fingers is of the order of  $10^6 \text{ m/s}^2$  and the RT wavelengths are between 10 to 50  $\mu\text{m}$  and increase as the primary KH wavelength become longer. During the start-up, the liquid jet is accelerated into the gas; RT instabilities appear at the rear side of the jet front. However, during shut-down the jet front decelerates. So, the lighter fluid is accelerating into the heavier fluid which is stabilizing on the rear side of the emerging jet and destabilizing on the jet front. A comparison between the computed RT wavelengths with classical linear instability theory shows a reasonable agreement. However, the measured wavelengths are longer compared to the theory due to the fact that the damping effects of viscosity on the smallest wavelengths have not been considered in the theory. The range of unstable wavelengths is consistent with VPF instability analysis that predicts stability for sub-micron and super millimeter wavelengths for the same fluid properties. Unstable wavelength increase up to 1200  $\mu\text{m}$  during the steady-state portion of injection that is larger compared to start-up. At higher  $We$  and  $Re$  numbers, smaller waves and thinner ligaments appear at the liquid/gas interface.

To tackle the resolution problem and capture the shortest unstable surface wavelengths, a new model has been developed to examine stream-wise segments of the jet during transients. The frame of reference has been transferred from the laboratory frame to an accelerating frame fixed to the liquid. This transformation generates a new term as a generalized body force analogous to gravity in equations of motion. The magnitude of the acceleration is derived from full transient jet computations. Periodic conditions fore and aft of the segment are used in this liquid-segment model.

The initial disturbances at the interface, i.e., 70-120  $\mu\text{m}$  grow and thin ligaments form at the interface as the gas accelerates above the liquid. RT wavelengths about 10-20  $\mu\text{m}$  sit at the back of these fingers similar to the scenario described for the full jet. Increasing the magnitude of the accelera-

tion leads to longer and thinner ligaments drawn out of the liquid for higher  $We$  numbers. The KH wavelengths become as long as  $200\ \mu\text{m}$  as the boundary layers develop in both phases and the secondary instability waves become longer, i.e.,  $20\text{-}35\ \mu\text{m}$ . Therefore, the RT instability is not independent of the KH instability for the transient liquid jet. The nonlinear synergism between the longer, highly distorted KH surface waves and the shorter RT waves explains the experimental results that droplet sizes are usually smaller than KH wavelengths and very close to the RT wavelengths appear as a secondary instability on top of KH instability. The range of unstable wavelengths and the unstable structures appearing at the liquid/gas interface repeat the scenario described for full transient jet.

## References

- [1] J. Y. Koo and J. K. Martin, “Droplet sizes and velocities in a transient Diesel fuel spray,” *SAE Tech. Paper*, no. 900397, 1990.
- [2] W. Cai, C. F. Powell, Y. Yue, S. Narayanan, J. Wang, M. W. Tate, M. J. Renzi, A. Ercan, E. Fontes, and S. M. Gruner, “Quantitative analysis of highly transient fuel sprays by time-resolved X-radiography,” *Appl. Phys. Lett.*, vol. 83, pp. 1671–1673, 2003.
- [3] W. Ning, R. Reitz, R. Diwakar, and A. Lippert, “A numerical investigation of nozzle geometry and injection condition effects on Diesel fuel injector flow physics,” *SAE Tech. Paper*, no. 2008-01-0936, 2008.
- [4] A. I. Ramirez, S. Som, S. K. Aggarwal, A. L. Kastengren, E. M. El-Hannouny, D. E. Longman, and C. F. Powell, “Characterizing spray behavior of common rail and heui injection systems using X-ray radiography,” *SAE World Congress, April 20-23, Detroit, Michigan*, 2009.
- [5] A. I. Ramirez, S. Som, S. K. Aggarwal, A. L. Kastengren, E. M. El-Hannouny, D. E. Longman, and C. F. Powell, “Quantitative X-ray measurements of high-pressure fuel sprays from a production heavy duty Diesel injector,” *Exp. Fluids*, vol. 47, pp. 19–134, 2009.
- [6] L. Pickett, S. Kook, and T. Williams, “Transient liquid penetration of early injection Diesel sprays,” *SAE Tech. Paper*, no. 2009-01-0839, 2009.

- [7] G. J. Smallwood, O. L. Gulder, and D. R. Snelling, “The structure of the dense core region in a transient Diesel spray,” *Symp. (Int.) on Comb.*, vol. 25, pp. 371–379, 1994.
- [8] O. L. Gulder, “Views on the structure of transient Diesel sprays,” *J. Atomiz. Sprays*, vol. 10, pp. 355–386, 2000.
- [9] D. J. Kim and J. K. Lee, “Analysis of the transient atomization characteristics of Diesel spray using time-resolved PDPA data,” *Int. J. Aut. Tech.*, vol. 9, pp. 297–305, 2008.
- [10] M. Linne, M. Paciaroni, T. Hall, and T. Parker, “Ballistic imaging of the near field in a Diesel spray,” *Exp. Fluids*, vol. 40, pp. 836–846, 2006.
- [11] A. L. Kastengren, C. F. Powell, T. Riedel, S.-K. Cheong, K.-S. Im, X. Liu, Y. J. Wang, and J. Wang, “Nozzle geometry and injection duration effects on Diesel sprays measured by X-ray radiography,” *J. Fluid Eng., Transaction of ASME*, vol. 130, no. 041301, 2008.
- [12] N. Abania and R. D. Reitz, “Unsteady turbulent round jets and vortex motion,” *Phys. Fluids*, vol. 19, pp. 125102–125113, 2007.
- [13] M. R. Turner, J. J. Healey, S. S. Sazhin, and R. Piazzesi, “Wave packet analysis and break-up length calculations for accelerating planar liquid jets,” *Fluid Dyn. Res.*, vol. 44, no. 015503, 2012.
- [14] M. R. Turner, S. S. Sazhin, J. J. Healey, C. Crua, and S. B. Martynov, “A break-up model for transient Diesel fuel sprays,” *Fuel*, vol. 19, pp. 288–305, 2012.
- [15] R. Aneja and J. Abraham, “How far does the liquid penetrate in a Diesel engine: Computed results vs. measurements,” *Combust. Sci. and Tech.*, vol. 138, pp. 233–255, 1998.
- [16] M. Herrmann, “A balanced force Refined Level Set Grid Method for two-phase flows on unstructured flow solver grids,” *J. Comput. Phys.*, vol. 227, pp. 2674–2706, 2008.
- [17] M. Goroshovski and M. Herrmann, “Modeling primary atomization,” *Annu. Rev. Fluid Mech.*, vol. 40, pp. 343–366, 2008.

- [18] C. M. Varga, J. C. Lasheras, and E. J. Hopfinger, “Initial breakup of a small- diameter liquid jet by a high-speed gas stream,” *J. Fluid Mech.*, vol. 497, pp. 405–434, 2003.
- [19] D. D. Joseph, A. Huang, and G. V. Candler, “Vaporization of a liquid drop suddenly exposed to a high-speed airstream,” *J. Fluid Mech.*, vol. 318, pp. 223–236, 1996.
- [20] D. D. Joseph, J. Belanger, and G. S. Beavers, “Breakup of a liquid drop suddenly exposed to a high-speed airstream,” *Int. J. Multiphase Flow*, vol. 25, pp. 1263–1303, 1999.
- [21] T. Funada and D. D. Joseph, “Viscous potential flow analysis of Kelvin-Helmholtz instability in a channel,” *J. Fluid Mech.*, vol. 445, pp. 263–283, 2001.
- [22] D. D. Joseph, T. Funada, and J. Wang in *Potential Flows of Viscous and Viscoelastic Liquids*, Cambridge University Press, 2008.
- [23] J. Han and G. Tryggvason, “Secondary breakup of axisymmetric liquid drops. I. acceleration by a constant body force,” *Phys. Fluids*, vol. 11, pp. 3650–3667, 1999.
- [24] S. Dabiri, W. A. Sirignano, and D. D. Joseph, “Cavitation in an orifice flow,” *Phys. Fluids*, vol. 19, no. 072112, 2007.
- [25] S. Dabiri, W. A. Sirignano, and D. D. Joseph, “Two-dimensional and axisymmetric viscous flow in apertures,” *J. Fluid Mech.*, vol. 605, pp. 1–18, 2008.
- [26] S. Dabiri, *Effects of Cavitation on High Pressure Atomization*. PhD thesis, University of California, Irvine, 2009.
- [27] T. Hayase, J. A. C. Humphrey, and R. Greif, “A consistently formulated QUICK scheme for fast and stable convergence using finite-volume iterative calculation procedure,” *J. Comput. Phys.*, vol. 98, pp. 108–118, 1992.
- [28] S. V. Patankar in *Numerical Heat Transfer and Fluid Flow*, Hemisphere, 1980.

- [29] M. Sussman, E. Fatemi, P. Smereka, and S. Osher, “An improved level set method for incompressible two-phase flows,” *Comput. Fluids*, vol. 27, pp. 663–680, 1998.
- [30] F. R. P. Osher, S., “Level set methods: an overview and some recent results,” *J. Comput. Phys.*, vol. 169, pp. 436–502, 2001.
- [31] D. Jarrahbashi, W. A. Sirignano, and S. Dabiri, “Transient high-pressure fuel injection processes,” in *ILASS Meeting, Ventura, CA*, May 2011.
- [32] S. Chandrasekhar in *Hydrodynamic and Hydromagnetic Stability*, Clarendon, 1961.
- [33] P. Marmottant and E. Villermaux, “On spray formation,” *J. Fluid Mech.*, vol. 498, pp. 73–111, 2004.
- [34] E. Villermaux and C. Clanet, “Life of a flapping liquid sheet,” *J. Fluid Mech.*, vol. 462, pp. 341–363, 2002.
- [35] L. Rayleigh, “On the stability, or instability of certain fluid motion-incompressible heavy fluid of variable density spray formation,” *Proc. R. Soc.*, vol. 11, p. 57, 1880.
- [36] G. I. Taylor, “Investigation of the character of the equilibrium of an incompressible heavy fluid of variable density spray formation,” *Proc. R. Soc. LOND. A*, vol. 201, pp. 192–196, 1950.
- [37] L. Rayleigh, “Investigation of the character of the equilibrium of an incompressible heavy fluid of variable density spray formation,” *Proc. R. Soc.*, vol. 14, pp. 170–177, 1883.
- [38] G. S. Jiang and D. Peng, “Weighted ENO schemes for Hamilton-Jacobi equations,” *SIAM J. Sci. Comput.*, vol. 21, pp. 2126–2143, 1997.